Astroparticle Physics

Lectures:

05.02.2019 1. Historical introduction, basic properties of cosmic rays
07.02.2019 2. Hadronic interactions and accelerator data
19.02.2019 3. Cascade equations
21.02.2019 4. Electromagnetic cascades
26.02.2019 5. Extensive air showers
28.02.2019 6. Detectors for extensive air showers
09.04.2019 7. High energy cosmic rays and the knee in the energy spectrum of cosmic rays
16.04.2019 8. Radio detection of extensive air showers
25.04.2019 9. Acceleration, astrophysical accelerators and beam dumps
07.05.2019 10. Extragalactic propagation of cosmic rays
16.05.2019 11. Ultra high energy cosmic rays
21.05.2019 12. Astrophysical gamma rays and neutrinos
28.05.2019 13. Neutrino astronomy
04.06.2019 14. Gamma-ray astronomy

http://particle.astro.ru.nl/goto.html?astropart1819

lecture 9
Acceleration, Astrophysical accelerators and beam dumps

Gaisser chapter 12

12.1 Power

There are two aspects to the question of cosmic ray acceleration: what is the source of power for the accelerators and what is the actual mechanism. From the discussion of Figure 1.5 we recall that the energy density in cosmic rays locally is $\rho_E \approx 0.5$ eV/cm^3. Taking account of the energy-dependent escape time for cosmic rays and assuming a uniform distribution of sources in the disk, we estimated in Section 9.3.2 the power requirement as

$$L_{\rm CR} = 7 \times 10^{40} \frac{\rm erg}{\rm sec} \equiv \frac{V_D \rho_E}{\tau_R}. \qquad (12.2)$$

It was emphasized long ago by Ginzburg and Syrovatskii [359] that the power requirement of Eq. 12.2 is suggestive of supernovae. For example, for 10 $M_\odot$ ejected from a type II supernova with a velocity $u \sim 5 \times 10^8$ cm/s every 30 years,

$$L_{\rm SN} \sim 3 \times 10^{42} \, {\rm erg/s}. \qquad (12.3)$$

There are large uncertainties in these numbers, but it appears plausible that an efficiency of a few per cent would be enough for supernova blast waves to energize all the galactic cosmic rays. Note that by terrestrial standards this is *very* efficient indeed. Such high efficiencies may be natural in space where there is no need to cool magnets and where particle acceleration may in fact be a major source of energy dissipation.

12.2.1 Fermi mechanism

Fermi acceleration works by transferring macroscopic kinetic energy of moving magnetized plasma to individual charged particles, thereby increasing the energy per particle to many times its original value and achieving the non-thermal energy distribution characteristic of cosmic ray protons and nuclei. Consider a process in which a test particle increases its energy by an amount proportional to its energy with each "encounter" (to be defined later). Then, if $\Delta E = \xi E$ per encounter, after n encounters

$$E_n = E_0 (1 + \xi)^n, \tag{12.4}$$

where E_0 is the energy at injection into the accelerator. If the probability of escape from the acceleration region is P_{esc} per encounter, then the probability of remaining in the acceleration region after n encounters is $(1 - P_{esc})^n$. The number of encounters needed to reach energy E is, from Eq. 12.4,

$$n = \ln(\frac{E}{E_0}) / \ln(1 + \xi). \tag{12.5}$$

Thus, the proportion of particles accelerated to energies greater than E is given by summing all encounters with $m \geqslant n$ as

$$N(\geqslant E) \propto \sum_{m=n}^{\infty} (1 - P_{\rm esc})^m = \frac{(1 - P_{\rm esc})^n}{P_{\rm esc}}, \tag{12.6}$$

with n given by Eq. 12.5. Substitution of 12.5 into 12.6 gives

$$N(> E) \propto \frac{1}{P_{\rm esc}} \left(\frac{E}{E_0}\right)^{-\gamma}, \tag{12.7}$$

with

$$\gamma = \ln\left(\frac{1}{1 - P_{\rm esc}}\right) / \ln(1 + \xi) \approx \frac{P_{\rm esc}}{\xi} = \frac{1}{\xi} \times \frac{T_{\rm cycle}}{T_{\rm esc}}. \tag{12.8}$$

The Fermi mechanism leads to the desired power law spectrum of energies. The last step of Eq. 12.8 introduces the characteristic time for the acceleration cycle, $T_{\rm cycle}$, and the characteristic time for escape from the acceleration region, $T_{\rm esc}$. The ratio of these two times is the probability per encounter of escape from the acceleration region. After the acceleration process has been working for a time t, $n_{\rm max} = t/T_{\rm cycle}$ and

$$E \leqslant E_0 (1 + \xi)^{t/T_{\rm cycle}}. \tag{12.9}$$

The Fermi mechanism leads to the desired power law spectrum of energies. The last step of Eq. 12.8 introduces the characteristic time for the acceleration cycle, $T_{\rm cycle}$, and the characteristic time for escape from the acceleration region, $T_{\rm esc}$. The ratio of these two times is the probability per encounter of escape from the acceleration region. After the acceleration process has been working for a time t, $n_{\rm max} = t/T_{\rm cycle}$ and

$$E \leqslant E_0 (1 + \xi)^{t/T_{\rm cycle}}. \qquad (12.9)$$

Two characteristic features of Fermi acceleration are apparent from Eq. 12.9. First, higher-energy particles take longer to accelerate than low-energy particles. Second, if a certain kind of Fermi accelerator has a limited lifetime, $T_{\rm A}$, then it will also be characterized by a maximum energy per particle that it can produce. This would be given by Eq. 12.9 with $t = T_A$ if $T_{\rm cycle}$ were independent of energy, which, however, turns out not to be the case for acceleration by supernovas, as we discuss later in this chapter.

12.2.2 *First- and second-order Fermi acceleration*

Diffusion of charged particles in turbulent magnetic fields physically carried along with moving plasma is the mechanism for energy gains and losses. In his original paper, Fermi [365] considered encounters with moving clouds of plasma, as illustrated in Figure 12.1. A particle with energy E_1 goes into the cloud where it begins to diffuse by "scattering" on the irregularities in the magnetic field. ("Scattering" is in quotes here because the process must be "collisionless" in terms of interactions between particles that would prevent acceleration because of collisional energy loss.) The result of the diffusion inside the gas cloud is that, after a few "scatterings" the *average* motion of the particle coincides with that of the gas cloud. In the rest frame of the moving gas the cosmic ray particle has total energy (rest mass plus kinetic)

$$E_1' = \Gamma E_1 (1 - \beta \cos\theta_1). \tag{12.10}$$

where Γ and $\beta \equiv V/c$ are the Lorentz factor and velocity of the cloud and the primes denote quantities measured in a frame moving with the cloud. All the "scatterings" inside the cloud are due to motion in the magnetic field and are therefore elastic. Thus, the energy of the particle in the moving frame just before it escapes is $E_2' = E_1'$. If we transform this energy back to the lab frame, we have the energy of the particle after its encounter with the cloud,

$$E_2 = \Gamma E_2' (1 + \beta \cos\theta_2'). \tag{12.11}$$

On the Origin of the Cosmic Radiation

ENRICO FERMI
Institute for Nuclear Studies, University of Chicago, Chicago, Illinois
(Received January 3, 1949)

A theory of the origin of cosmic radiation is proposed according to which cosmic rays are originated and accelerated primarily in the interstellar space of the galaxy by collisions against moving magmetic fields. One of the features of the theory is that it yields naturally an inverse power law for the spectral distribution of the cosmic rays. The chief difficulty is that it fails to explain in a straightforward way the heavy nuclei observed in the primary radiation.

I. INTRODUCTION

IN recent discussions on the origin of the cosmic radiation E. Teller[1] has advocated the view that cosmic rays are of solar origin and are kept relatively near the sun by the action of magnetic fields. These views are amplified by Alfvén, Richtmyer, and Teller.[2] The argument against the conventional view that cosmic radiation may extend at least to all the galactic space is the very large amount of energy that should be present in form of cosmic radiation if it were to extend to such a huge space. Indeed, if this were the case, the mechanism of acceleration of the cosmic radiation should be extremely efficient.

I propose in the present note to discuss a hypothesis on the origin of cosmic rays which attempts to meet in part this objection, and according to which cosmic rays originate and are accelerated primarily in the interstellar space, although they are assumed to be prevented by magnetic fields from leaving the boundaries of the galaxy. The main process of acceleration is due to the interaction of cosmic particles with wandering magnetic fields which, according to Alfvén, occupy the interstellar spaces.

where H is the intensity of the magnetic field and ρ is the density of the interstellar matter.

One finds according to the present theory that a particle that is projected into the interstellar medium with energy above a certain injection threshold gains energy by collisions against the moving irregularities of the interstellar magnetic field. The rate of gain is very slow but appears capable of building up the energy to the maximum values observed. Indeed one finds quite naturally an inverse power law for the energy spectrum of the protons. The experimentally observed exponent of this law appears to be well within the range of the possibilities.

The present theory is incomplete because no satisfactory injection mechanism is proposed except for protons which apparently can be regenerated at least in part in the collision processes of the cosmic radiation itself with the diffuse interstellar matter. The most serious difficulty is in the injection process for the heavy nuclear component of the radiation. For these particles the injection energy is very high and the injection mechanism must be correspondingly efficient.

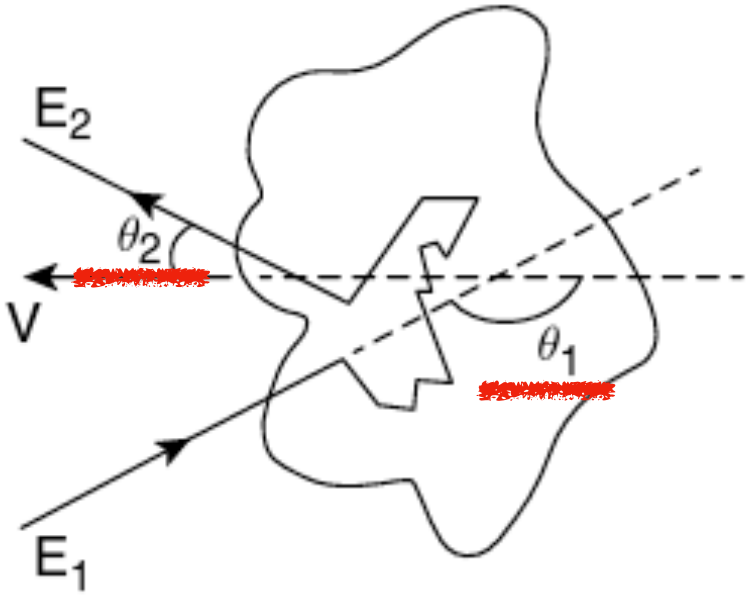

Figure 12.1 Acceleration by a moving, partially ionized gas cloud.

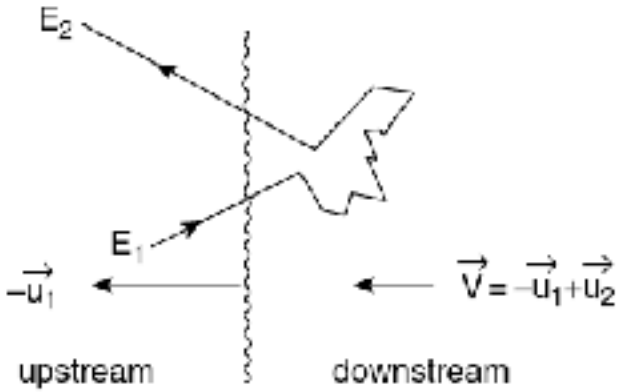

Figure 12.2 Acceleration at a plane shock front.

For simplicity, Eqs. 12.10 and 12.11 are written for a particle that is already sufficiently relativistic so that $E \approx pc$. Substituting Eq.12.10 into 12.11 now gives the energy change for the particular encounter characterized by θ_1 and θ_2,

$$\frac{\Delta E}{E_1} = \frac{1 - \beta\cos\theta_1 + \beta\cos\theta_2' - \beta^2\cos\theta_1\cos\theta_2'}{1 - \beta^2} - 1. \qquad (12.12)$$

The other physical situation that we want to consider is illustrated in Figure 12.2. Here a large, plane shock front moves with velocity $-\vec{u}_1$. The shocked gas flows away from the shock with a velocity $\vec{u}_2$ relative to the shock front, and $|u_2| < |u_1|$. Thus in the lab frame the gas behind the shock moves to the left with velocity $\vec{V} = -\vec{u}_1 + \vec{u}_2$. Eq. 12.12 applies also to this situation with $\beta = V/c$ now interpreted as the velocity of the shocked gas ("downstream") relative to the unshocked gas ("upstream").

The crucial difference between the two cases comes when we take the angular averages to obtain the average fractional energy gain per encounter, ξ, for Eqs. 12.4 to 12.9. The same steps will be followed in each case. In the equations that follow, we indicate scattering from clouds as case (**a**) and encounters with a plane shock front as (**b**). For plasma clouds

$$\textbf{(a)} \quad \frac{dn}{d\cos\theta_2'} = \text{constant}, \quad -1 \leqslant \cos\theta_2' \leqslant 1, \tag{12.13}$$

so that $\langle \cos\theta_2' \rangle_{\mathbf{a}} = 0$.

For a plane shock,

$$\textbf{(b)} \quad \frac{dn}{d\cos\theta_2'} = 2\cos\theta_2', \quad 0 \leqslant \cos\theta_2' \leqslant 1. \tag{12.14}$$

The distribution for case (b) is the normalized projection of an isotropic flux onto a plane, and $\langle \cos\theta_2' \rangle_{\mathbf{b}} = 2/3$.

Averaging Eq. 12.12 over $\cos\theta_2'$ for the two cases gives

$$\text{(a)}\quad \frac{\langle \Delta E\rangle_2}{E_1} = \frac{1-\beta\cos\theta_1}{1-\beta^2} - 1$$

and

$$\text{(b)}\quad \frac{\langle \Delta E\rangle_2}{E_1} = \frac{1-\beta\cos\theta_1 + \frac{2}{3}\beta - \frac{2}{3}\beta^2\cos\theta_1}{1-\beta^2} - 1. \qquad (12.15)$$

Next we need to average over $\cos\theta_1$. For clouds, the probability of a collision is proportional to the relative velocity between the cloud and the particle,

$$\frac{\mathrm{d}n}{\mathrm{d}\cos\theta_1} = \frac{c - V\cos\theta_1}{2c}, \quad -1 \leqslant \cos\theta_1 \leqslant 1, \qquad (12.16)$$

so that $\langle\cos\theta_1\rangle_{\mathbf{a}} = -V/3c$. The distribution of $\cos\theta_1$ for the plane shock is the projection of an isotropic flux onto a plane with $-1 \leqslant \cos\theta_1 \leqslant 0$, so that $\langle\cos\theta_1\rangle_{\mathbf{b}} = -2/3$. Thus

$$\text{(a)}\quad \xi = \frac{1+\frac{1}{3}\beta^2}{1-\beta^2} - 1 \sim \frac{4}{3}\beta^2$$

and

$$\text{(b)}\quad \xi = \frac{1+\frac{4}{3}\beta+\frac{4}{9}\beta^2}{1-\beta^2} - 1 \sim \frac{4}{3}\beta = \frac{4}{3}\frac{u_1-u_2}{c}. \qquad (12.17)$$

Here $\beta = V/c$ refers to the relative velocity of the plasma flow, not to the cosmic rays. The approximate forms in Eq. 12.17 hold when the shock (or cloud) velocities are non-relativistic.

Notice that in both cases an "encounter" is one pair of in and out crossings: in case (a) into and out of the cloud, and in case (b) back and forth across the shock. The original Fermi mechanism is second order in shock velocity β. On average, particles gain energy as in Eq. 12.17a, but in each encounter a particle can either gain or lose energy depending on the angles. This is often incorrectly expressed by saying that there are more approaching encounters ($\cos\theta_1 < 0$) than overtaking encounters ($\cos\theta_1 > 0$). But note from Eq. 12.12 that an approaching encounter with a cloud in which the particle goes out the back side ($\cos\theta_2' < 0$) can result in a loss of energy. Similarly, an overtaking collision can sometimes result in an energy gain. On the other hand, the geometry of the infinite plane shock is such that an "encounter" always results in an energy gain (because $\cos\theta_2'$ is always positive and $\cos\theta_1$ always negative). Because of the angular constraints, the term proportional to β in Eq. 12.15 does not cancel in this case, so acceleration at a large planar shock is first order in shock velocity.

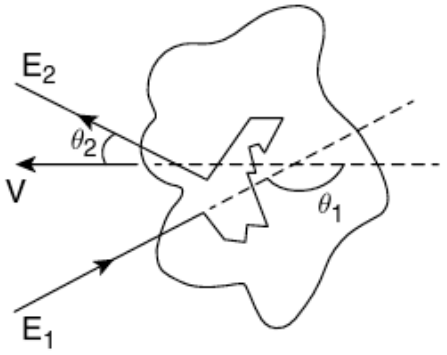

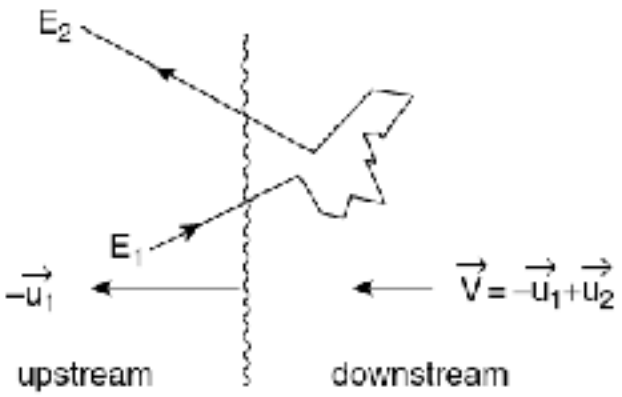

In the original version of Fermi acceleration, the acceleration region is the galactic disk, so $T_{esc} \sim 10^7$ years. The acceleration rate is the rate of collisions between a cosmic ray of velocity c with clouds characterized by a spatial density ρ_c and cross section σ_c. Thus $T_{cycle} \sim 1/(c\,\rho_c\,\sigma_c)$. The integral spectral index then is

$$\gamma \sim \frac{1}{\frac{4}{3}\beta^2 c\,\rho_c\,\sigma_c\,T_{acc}}. \tag{12.18}$$

The numerical value of this spectral index is not universal, but depends on details of properties of the clouds, and tends to be very large [366].

For the configuration of the large, plane shock, the rate of encounters is given by the projection of an isotropic cosmic ray flux onto the plane shock front,

$$\int_0^1 \mathrm{d}\cos\theta \int_0^{2\pi} \mathrm{d}\phi \frac{c\rho_{CR}}{4\pi}\cos\theta = \frac{c\rho_{CR}}{4}, \tag{12.19}$$

where ρ_{CR} is the number density of cosmic rays being accelerated. The rate of convection downstream away from the shock front is $\rho_{CR} \times u_2$, so

$$P_{esc} = \frac{\rho_{CR}\,u_2}{c\,\rho_{CR}/4} = \frac{4\,u_2}{c}. \tag{12.20}$$

Thus for the case of acceleration at a shock,

$$\gamma = \frac{P_{esc}}{\xi} = \frac{3}{u_1/u_2 - 1}. \tag{12.21}$$

Unlike the model for second-order Fermi acceleration, the spectral index here is independent of the absolute magnitude of the velocity of the plasma – it depends only on the ratio of the upstream and downstream velocities. Note that the spectral index is also independent of the diffusion coefficient. (As noted below, however, the upper limiting energy depends explicitly on the properties of diffusion.)

A shock can form when $u_1 > c_1$, the sound speed in the gas. The Mach number of the flow is $M = u_1/c_1$. The continuity of mass flow across the shock ($\rho_1 u_1 = \rho_2 u_2$), together with the kinetic theory of gases, gives

$$\frac{u_1}{u_2} = \frac{\rho_2}{\rho_1} = \frac{(c_p/c_v + 1)M^2}{(c_p/c_v - 1)M^2 + 2} \tag{12.22}$$

(Landau and Lifshitz [367]). For a monoatomic gas the ratio of specific heats is $c_p/c_v = \frac{5}{3}$, so

$$\gamma \approx 1 + \frac{4}{M^2} \tag{12.23}$$

for a strong shock with $M \gg 1$. Not only is the spectral index for first-order Fermi acceleration universal, but it has a numerical value close to what is needed to describe the observed cosmic ray spectrum! (Recall from the discussion in Chapter 9 that the differential spectral index required from the accelerator is $\sim 2.7 - \delta$, which corresponds to $\gamma \sim 1.7 - \delta$ in Eq. 12.23, where $0.3 \leqslant \delta \leqslant 0.6$.)

12.3 Acceleration at supernova blast waves

The ejected material from a supernova explosion moves out through the surrounding medium driving a shock wave ahead of the expanding SNR. As long as the characteristic length for diffusion, D/u, is much less than the radius of curvature of the shock, the plane approximation can be used. Thus the expanding supernova remnant is an ideal candidate for first-order Fermi acceleration as in Figure 12.2. While the SNR is in the initial free expansion phase the expanding shock overtakes the particles upstream and recycles them through the acceleration process, as described in the previous section.

As explained in the next chapter on supernovae, the characteristic time that marks the end of the free expansion phase is $T_{ST} \approx 1000$ yrs from Eq. 13.29 (for example with 10 $M_\odot$ expanding at mean velocity of 5×10^8 cm/s into a medium of average density 1 proton/cm^3). For times $t > T_{ST}$, in the Sedov–Taylor phase, the shock velocity decreases, and escape upstream can occur.

12.3.1 Maximum energy

During the free expansion phase, the acceleration rate is

$$\frac{\mathrm{d}E}{\mathrm{d}t} = \frac{\xi E}{T_{\mathrm{cycle}}}, \tag{12.24}$$

with the fractional energy gain per encounter, ξ, given by Eq. 12.17b. To integrate Eq. 12.24 and estimate E_{max}, we need to know the cycle time for one back-and-forth encounter. The following derivation is due to Lagage and Cesarsky [368] as presented by Drury [360].

Consider first the upstream region. The particle current with convection is given by

$$\vec{\mathbf{J}} = -D\vec{\nabla}N + \vec{\mathbf{u}}\,N. \tag{12.25}$$

In the upstream region the fluid velocity $\vec{\mathbf{u}}_1$ is negative relative to the shock front so in equilibrium there is no net current, and

$$D_1 \frac{\mathrm{d}N}{\mathrm{d}z} = -u_1\,N. \tag{12.26}$$

Then in the upstream region

$$N(z) = \rho_{CR} \exp[-z\, u_1 / D_1], \tag{12.27}$$

where ρ_{CR} is the number density of cosmic rays at the shock. The total number of particles per unit area in the upstream region is $\rho_{CR} D_1/u_1$. From Eq. 12.19 the rate per unit area at which relativistic cosmic rays cross a plane shock front is $c\,\rho_{CR}/4$. Thus the mean residence time of a particle in the upstream region is

$$(\rho_{CR}\, D_1/u_1)\,(c\,\rho_{CR}/4)^{-1} \;=\; 4\,D_1/(u_1\,c). \tag{12.28}$$

The downstream region is somewhat more complicated to analyze because it is necessary to average the residence time only over those particles that do not diffuse downstream out of the acceleration region. The analysis is straightforward and is shown explicitly by Drury. This form is identical to that in the upstream region. Thus

$$T_{cycle} \;=\; \frac{4}{c}\left(\frac{D_1}{u_1} - \frac{D_2}{u_2}\right). \tag{12.29}$$

To proceed we need an estimate of the diffusion coefficient. Lagage and Cesarsky argue that the diffusion length, λ_D cannot be smaller than the Larmor radius of the particle, $r_L = pc/(ZeB)$, where Z is the charge of the particle and p its total momentum. The idea is that energetic particles cannot respond to irregularities in the magnetic field smaller than the particle gyroradius. Then the minimum diffusion coefficient is

$$D_{\rm min} = \frac{r_L\, c}{3} \sim \frac{1}{3}\frac{E\, c}{Z\, e\, B}, \tag{12.30}$$

so that $T_{\rm cycle} \geqslant 20\, E/(3u_1 Z\, e\, B)$ for a strong shock with $u_2 = u_1/4$. Here E is the total energy of the nucleus being accelerated. Inserting $D_1 = D_2 = D_{\rm min}$ into Eqs. 12.29 and 12.24 leads to an expression for the acceleration rate that is independent of energy because $T_{\rm cycle} \propto E$.

The resulting estimate of the maximum energy is

$$E_{\rm max} \leqslant \frac{3}{20}\frac{u_1}{c} Z\, e\, B\, (u_1\, T_A) \tag{12.31}$$

with $T_A = T_{\rm ST} \sim 1000$ years. An estimate of $B_{\rm ISM} \sim 3\mu$G in Eq. 12.31 then gives

$$E_{\rm max} \leqslant Z \times 3 \times 10^4 \text{ GeV}. \tag{12.32}$$

The Lagage & Cesarsky [368] estimate of the maximum energy for acceleration by SNR is now thought to be low by a factor of 30 to 100 because the magnetic field in the acceleration region is amplified by nonlinear effects in the acceleration process. (See Section 12.5 below.)

12.5 The knee of the cosmic ray spectrum

The numerical value of the maximum energy in Eq. 12.32 of $E_{max} \approx Z \times 3 \times 10^4$ GeV is obtained under the assumption that the magnetic field strength in the acceleration region is 3 μG, similar to that in the ISM. Over the past decade both theoretical and observational evidence indicates that the magnetic fields may be significantly higher in supernova shocks than in the interstellar medium. The amplification of the magnetic field is another consequence of the nonlinear interaction between the particles being accelerated and the plasma in the region of the shock, as shown in theoretical work by Bell [376] and others. The theory of magnetic field amplification is beyond the scope of this book. However, some qualitative insight into the problem may be obtained from Figure 9.1 (e, f and g). When the energy in the accelerated particles streaming ahead of the shock is comparable to the energy of the magnetic fields threading the upstream plasma, resonant effects may be expected to amplify the magnetic fields.

The observational evidence is in the form of narrow filaments of synchrotron radiation associated with shocks in young supernova remnants such as SN 1006. Quantitative interpretation of the observations leads to the conclusion that magnetic fields at the shocks of young supernova remnants are of order 100 μG [377]. If so, this would put the maximum energy close to or in the energy region about 1 PeV where the spectrum steepens at the knee. One would then associate the knee with the beginning of the end of the population of galactic cosmic rays. Since $E_{\max} \propto Z$, there would be a corresponding evolution of the spectrum toward increasingly heavier nuclei when the spectrum is measured as total energy per particle, as in air shower experiments. The successive cutoff of protons, helium, CNO, Mg-Si and Fe in this situation was first pointed out in [26], and is sometimes referred to as a "Peters cycle." Models for the evolution of cosmic ray composition based on this idea [28] are currently used to relate air-shower measurements of the all-particle spectrum to the spectrum of nucleons needed to calculate the inclusive flux of atmospheric muons and neutrinos [264].

Observation of such a composition cycle does not necessarily imply that the knee is due to the maximum energy of the acceleration mechanism. For example, if there is rigidity-dependent leakage from the galaxy that increases with energy in this region, this also would give an increasingly heavy composition associated with a steepening of the measured all particle energy per nucleus spectrum. A recent paper of Giacinti et al. [378] attributes the knee entirely to propagation effects. More likely, both effects play a role.

The Astrophysical Journal, 790:85 (16pp), 2014 August 1 doi:10.1088/0004-637X/790/2/85

MAGNETIC FIELD AMPLIFICATION IN THE THIN X-RAY RIMS OF SN 1006

Sean M. Ressler[1], Satoru Katsuda[2], Stephen P. Reynolds[3], Knox S. Long[4], Robert Petre[5], Brian J. Williams[5], and P. Frank Winkler[6]

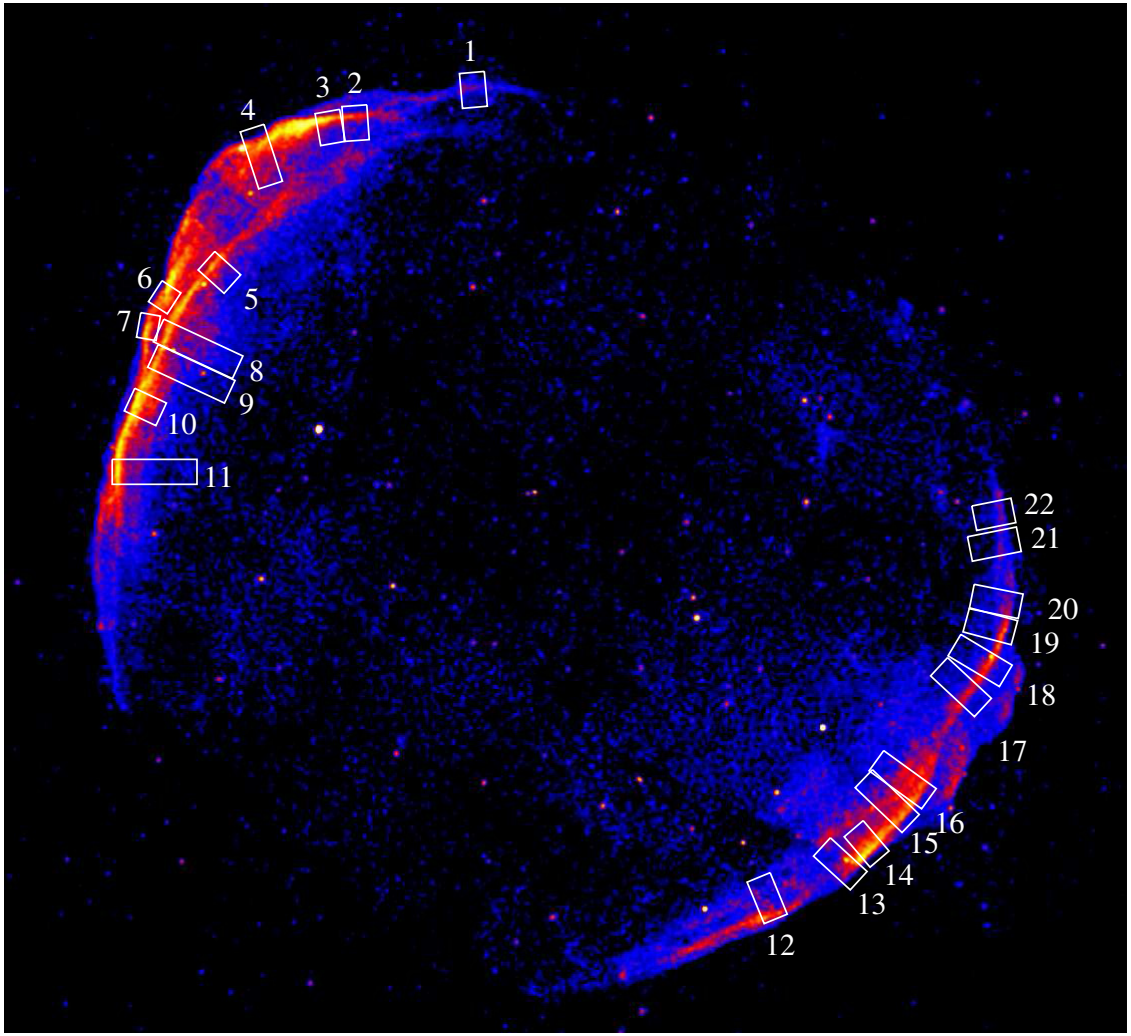

Figure 7. *Chandra* image at 2–7 keV showing the regions where radial profiles were extracted. Filament 1: Regions 1–4 and 6; Filament 2: Regions 5, 7, and 9–11; Filament 3: Regions 12–16; Filament 4: Regions 17–22; Filament 5: Regions 6 and 8.

12.6 Acceleration to higher energy

The maximum energy from shock acceleration by a supernova remnant as written in Eq. 12.31 can be reformulated

$$E_{\max} = \text{const} \times \beta\, Ze\, B\, R, \tag{12.65}$$

where $R = u_1 \times T_A$ is the radius at the time when the expansion begins to slow down. This result is an instance of a more general consideration in which the energy is limited by the gyroradius in the accelerator, $r_L = E/ZeB$. Then $r_L < R$ gives $E < Ze\, B\, R$. In a classic paper, Hillas [379] drew attention to the practical implications of this condition by placing then known potential sources of cosmic rays on a diagram of magnetic field strength versus size. We show the original Hillas plot as Figure 12.7. At the time, GRBs were not yet understood, but they are an important addition to the plot in a similar region to AGN.

It is interesting to note that active galaxies appear in two regions of the Hillas plot: as active galactic nuclei and as radio galaxy lobes. Acceleration of cosmic rays to approaching 10^{20} eV is possible in both locations, but the implications for secondary radiation of gamma rays and neutrinos are quite different in the two cases. If, as [381] prefers, the UHECR are accelerated at the termination shocks far out from the AGN, then there would be little target material and not much opportunity for producing neutrinos and gamma rays of hadronic origin. If the acceleration occurs primarily in the jets near the central black hole or somewhat further out, but still inside the jets where there are intense radiation fields for photo-pion production, then conditions for production of hadronic secondaries are more favorable. The two possibilities are illustrated in Figure 12.8.

Acceleration to higher energy will be discussed in the following chapters in connection with the various possible sources and in Chapter 17 in connection with cosmic rays of extragalactic origin.

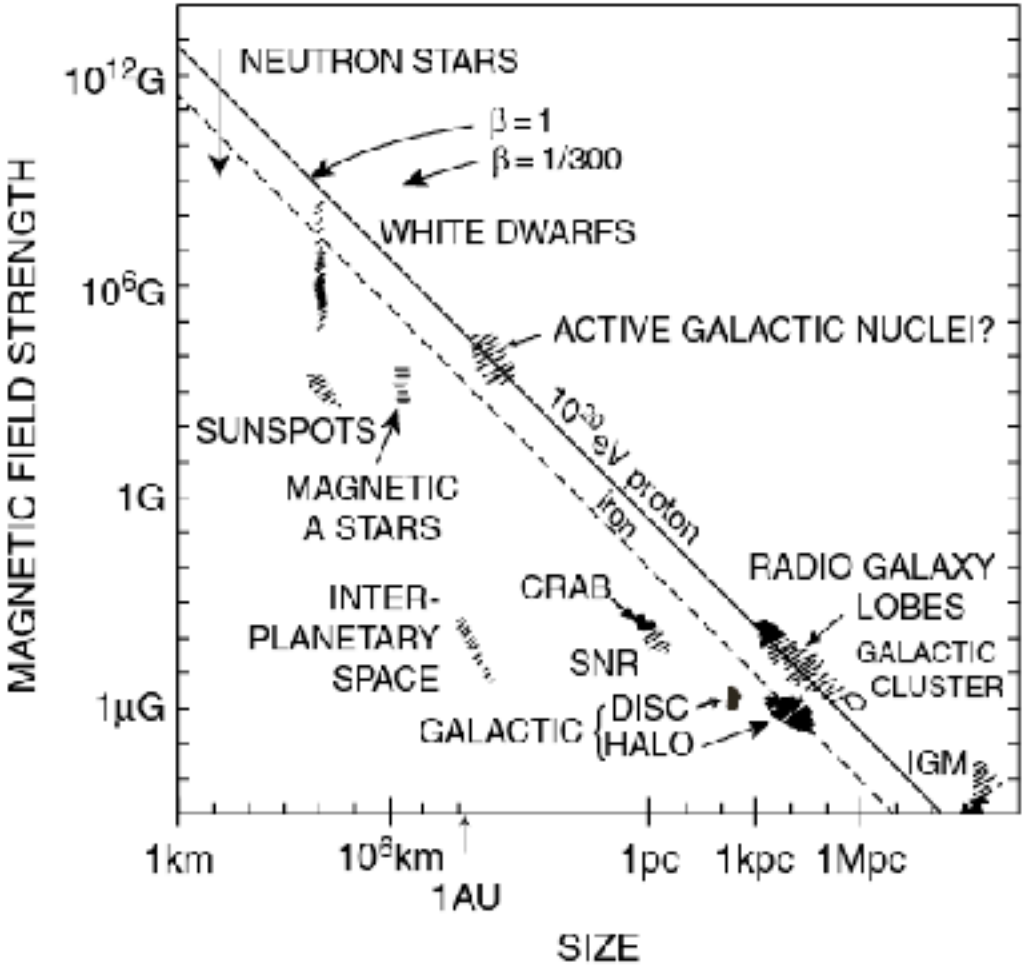

Figure 12.7 The Hillas Plot of potential cosmic ray accelerators locates objects according to size and magnetic field. Objects to the left of the diagonals cannot accelerate particles to 10^{20} eV total energy. Separate lines are shown for protons (solid) and iron (broken), and the shaded region shows the effect of shock velocity. From [379], © 1984 by Annual Reviews (www.annualreviews.org), reproduced with permission.

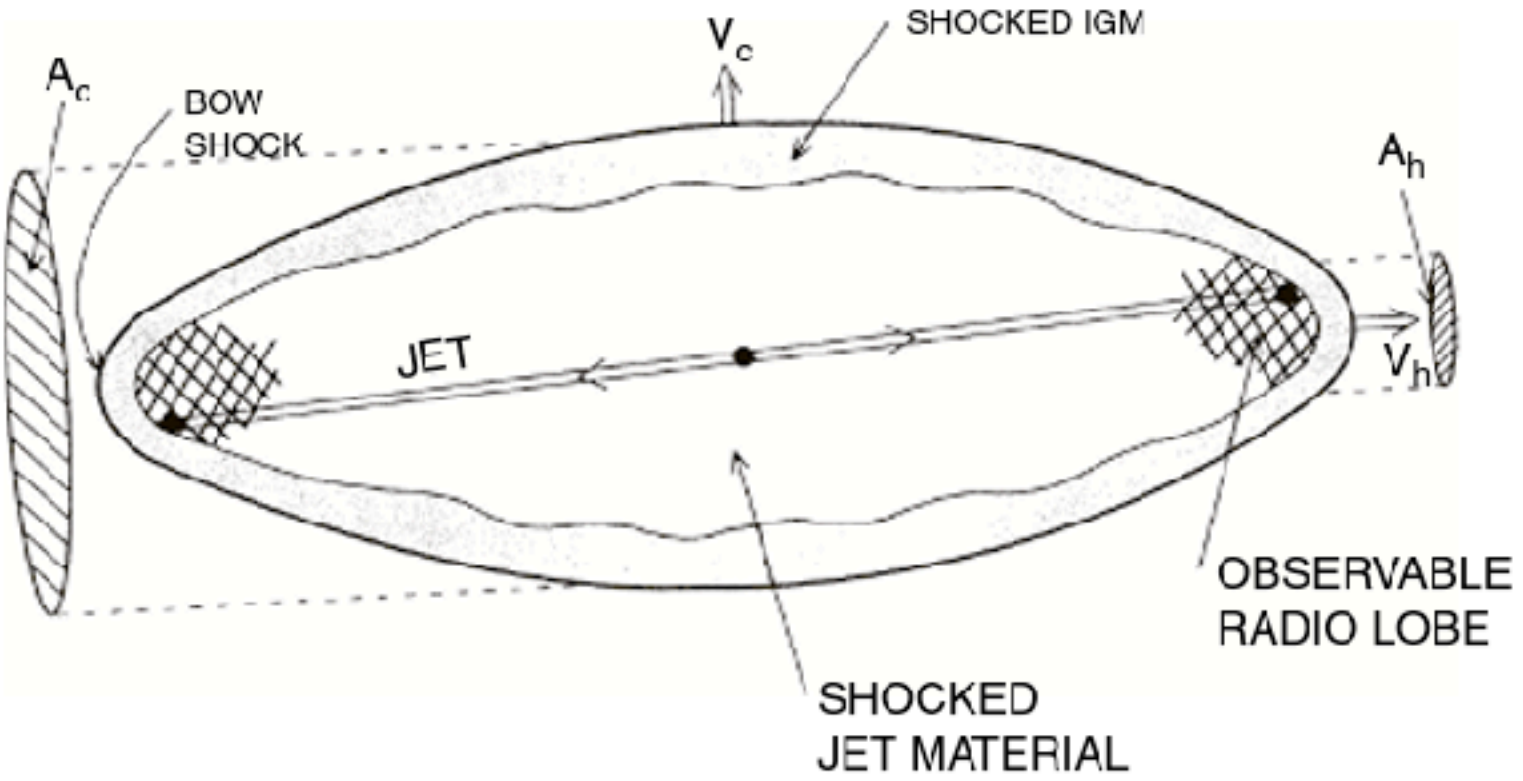

Figure 12.8 Diagram showing the termination shock or "cocoon" of an active galaxy. From [380], © 1989 by American Astronomical Society, reproduced with permission.

lecture 9
Acceleration, Astrophysical accelerators and beam dumps

Gaisser chapter 14

Cosmic rays (electrons and protons) accelerated in cosmic sites can be studied through the investigation of their secondary products (photons and neutrinos). Photons are produced by radiation from charged particles and from decay of pions produced by interactions of protons with target material present inside or close by the accelerator. High-energy neutrinos are produced only via hadronic interactions. We describe in this chapter the radiative processes and the astrophysical scenarios in which the condition for efficient acceleration (source) and interaction (target) are satisfied. We call these configurations "astrophysical beam dumps." The analogy is to a beam dump at a terrestrial accelerator in which all possible secondaries are produced. Secondary photons and neutrinos from a cosmic accelerator point back to their source allowing the identification of high-energy accelerators.

14.1 Radiative processes in beam dumps

The spectrum of a beam dump is usually measured as the energy (in erg or eV) per unit frequency ν (in Hz) passing a surface (cm^2) in a second. It is described as a power law with *flux density*

$$f(\nu) \equiv F_\nu \propto \nu^{-s} \tag{14.1}$$

with units erg cm^{-2} s^{-1} Hz^{-1}. The spectral index s is of importance for the characterization of the source. Another important quantity is the *energy flux* (νF_ν), usually expressed in erg cm^{-2} s^{-1}. The function νF_ν for an object is called its *spectral energy distribution* (SED).

Equivalently, the spectrum can be also expressed as *spectral photon (neutrino) flux* or number of photons (neutrinos) per energy unit E

$$N(E) = \mathrm{d}N/\mathrm{d}E \propto E^{-(s+1)} \tag{14.2}$$

in GeV ^{1} cm^{-2} s^{-1}. The photon (or neutrino) flux is related to the energy flux as

$$\nu F_\nu = E^2 \mathrm{d}N/\mathrm{d}E. \tag{14.3}$$

Later in this chapter, we will show several examples of SEDs of gamma rays from distant sources measured at Earth (Figures 14.5 to 14.7). For a cosmologically nearby source at a distance d, the measured SED and the corresponding intrinsic differential luminosity at the source are related by

$$\nu F_\nu = \frac{L_\nu}{4\pi d^2}, \tag{14.4}$$

assuming isotropic emission. In general it is necessary to account for the expansion of the Universe in making the connection. In terms of the total luminosity L at the source, the relation is

$$\Phi = \int \frac{\nu F_\nu}{E} \mathrm{d}E = \frac{L}{4\pi D_L^2}, \tag{14.5}$$

where Φ is the total measured integrated energy flux and $D_L(z)$ is the luminosity distance, see Appendix A.11.

14.1.1 Synchrotron radiation

The importance of the synchrotron radiation in astrophysics was first identified by Shklovskii in 1957 in the study of the non-thermal spectrum of the Crab supernova remnant [442]. It has since been used to analyze a variety of astrophysical environments. Most of the radiation in the radio to soft X-ray band from sources such as accreting black holes is synchrotron radiation from accelerated electrons in strong magnetic fields. The spectrum of the electromagnetic radiation that is produced depends on the spectrum of the radiating electrons. If the source region is dense, the radiation will be partially absorbed inside the source. In addition, the energetic electrons can interact with the synchrotron photons and produce a higher energy population of photons by inverse-Compton scattering. The three processes are indicated schematically in Figure 14.1.

An electron with charge e and velocity v moving in a magnetic field B feels an external force [443]

$$\vec{F} = \frac{\mathrm{d}}{\mathrm{d}t}(\gamma\, m_e\, \vec{v}) = \frac{e}{c}(\vec{v} \times \vec{B}) = m_e \gamma \frac{\mathrm{d}\vec{v}}{\mathrm{d}t}, \tag{14.6}$$

where γ here is the Lorentz factor of the electron. The last step in Eq. 14.6 follows in the absence of electric fields since the magnetic force is always perpendicular to the motion of the electron. In this case, γ is constant and the electron follows a helical trajectory with rotation frequency

$$\nu_B = \frac{\nu_C}{\gamma} = \frac{Be}{2\pi\, \gamma m_e}, \tag{14.7}$$

where the Lorentz factor of the electron is related to its speed by

$$\gamma = \frac{1}{\sqrt{1 - (\frac{v}{c})^2}}. \tag{14.8}$$

For non-relativistic electrons, ν_C is also the frequency of the electromagnetic radiation.

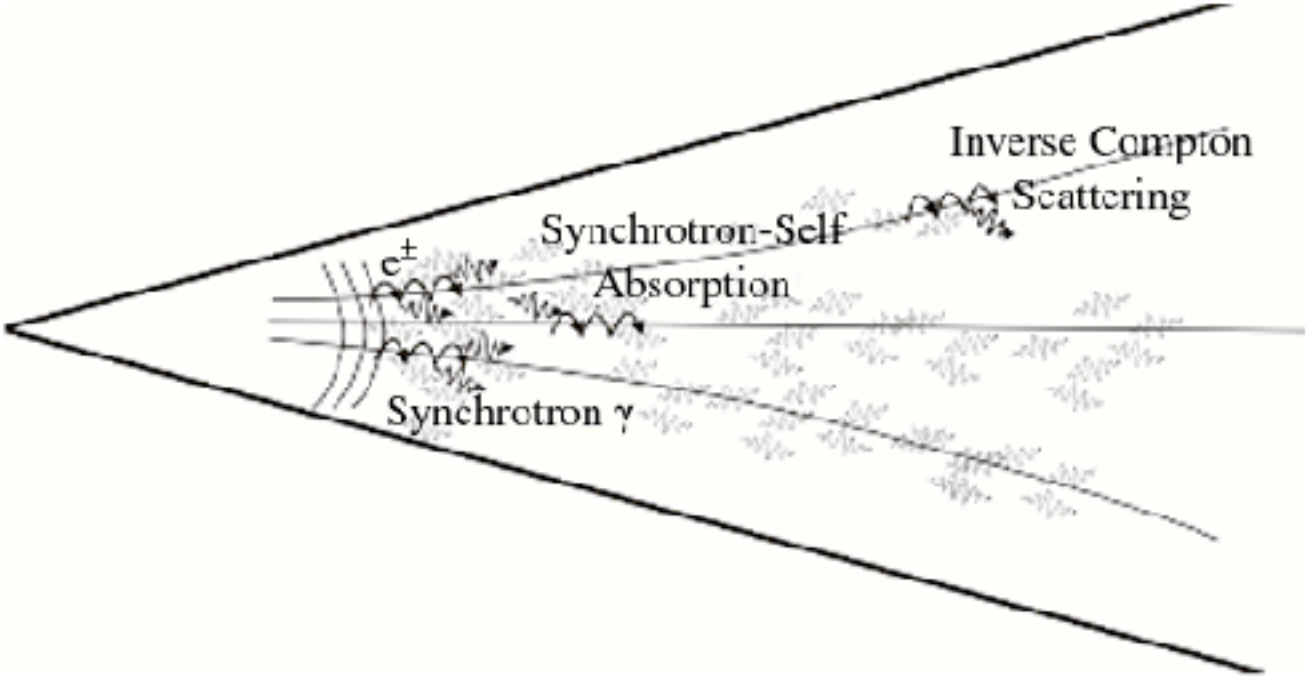

Figure 14.1 Scheme of the principle mechanisms involved in the self-synchrotron model.

The situation is more complicated for relativistic electrons, and the details are fully explained in the book by Rybicki and Lightman [443]. A relativistic electron in a magnetic field has a radiation pattern peaked in the direction of motion of the electron, which is changing as the particle bends in the magnetic field. The observer sees a spectrum of radiation peaked at

$$\nu_S = \gamma^3 \nu_B = \gamma^2 \nu_C. \tag{14.9}$$

ν_S is called *synchrotron frequency* and the electromagnetic radiation emitted is called *synchrotron radiation (SR)*. The energy of the electron is $E = \gamma m_e c^2$; hence the synchrotron frequency is related to the energy of the electron by

$$\nu_S \propto B\, E^2. \tag{14.10}$$

It can be shown that the spectrum of synchrotron radiation of a single electron is sharply peaked near the synchrotron frequency ν_S and that the electrons lose energy at the rate

$$\mathrm{d}E/\mathrm{d}t \propto E^2\, B^2. \tag{14.11}$$

Averaging over the direction between the velocity of the electron and the direction of the magnetic field, the power radiated per electron is

$$\left(-\frac{\mathrm{d}E}{\mathrm{d}t}\right)_{\mathrm{synch}} = \frac{\sigma_{\mathrm{T}} c}{6\pi} \gamma^2 B^2, \tag{14.12}$$

where σ_{T} is the Thomson cross section; see Appendix A.1.

All charged particles radiate when moving across a magnetic field. From Eq. 14.12 we see that the power radiated in a given magnetic field is proportional to the fourth power of the electric charge of the particle and to the square of its Lorentz factor and inversely proportional to the square of the particle mass. Since the Lorentz factor is also inversely proportional to the mass of the particle, the radiation from a particle with mass m and unit charge will be suppressed relative to that of an electron of the same energy by $(m_e/m)^4$. Because of the strong dependence on mass, synchrotron radiation is unimportant for protons except in the most extreme environments. Despite this, synchrotron radiation from protons is important to account for GeV–TeV photons in lepto-hadronic models of blazars, as discussed in the next section.

The spectral distribution of synchrotron radiation from a single electron is described by two functions corresponding to polarization parallel and perpendicular to the direction of the magnetic field. The power radiated per unit frequency is the sum of the contributions from the two polarizations. This function depends on the ratio $x = \nu/\nu_S$ and has the asymptotic forms

$$F(x) \approx \begin{cases} F_1\, x^{1/3} & \text{for } x \ll 1 \\ F_2\, e^{-x}\, x^{1/2} & \text{for } x \gg 1. \end{cases} \tag{14.13}$$

The function is strongly peaked near the synchrotron frequency, as shown in Figure 14.2.

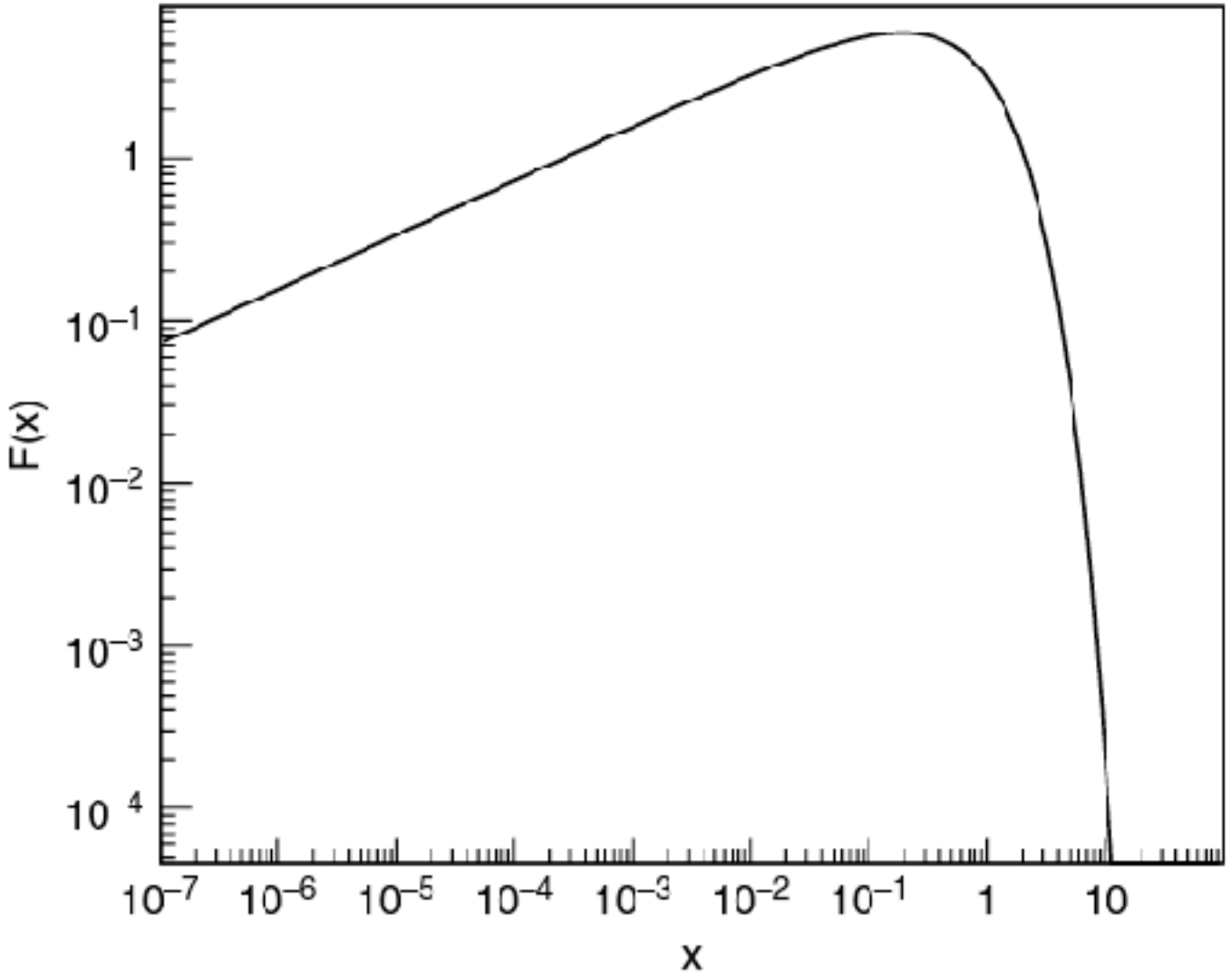

Figure 14.2 Asymptotic formula for the synchrotron function $F(x)$. Fitted parameters taken from [444].

The next step is to generalize from the case of the single electron to an ensemble of particles distributed as a power-law, which is a more representative case for common astrophysical environments. The derivation is given in [443] and [445]. The number density of electrons with energy between E and $E+\mathrm{d}E$ is

$$\frac{\mathrm{d}N(E)}{\mathrm{d}E} = kE^{-p} \propto \gamma^{-p}, \tag{14.14}$$

and the power radiated at frequency ν by electrons with energy E is proportional to $F(\nu/\nu_S)$ with $\nu_S = \gamma^2 \nu_C$. The frequency distribution of the radiation from the spectrum of electrons is therefore

$$f(\nu) \propto \int \gamma^{-p} F(\nu/\nu_S)\mathrm{d}\gamma. \tag{14.15}$$

Changing the variable of integration to $x = \nu/\nu_S = \nu/(\gamma^2\nu_C)$, the integral becomes

$$f(\nu) \propto \left(\frac{\nu}{\nu_C}\right)^{-(p-1)/2} \int x^{(p-3)/2} F(x)\mathrm{d}x. \tag{14.16}$$

Thus

$$f(\nu) \propto \nu^{-s} \text{ with } s = \frac{p-1}{2}. \tag{14.17}$$

The synchrotron flux from a source of volume $V \propto R^3$ at a distance d is

$$F_S(\nu) \propto \frac{R^3}{d^2} k B^{1+s} \nu^{-s}, \tag{14.18}$$

which implies that observing a source at two different frequencies allows one to determine the slope of the particle energy distribution s.

Synchrotron self-absorption

The observer sees a synchrotron spectrum $F_S(\nu) \propto \nu^{-s}$ only if no absorption of photons by the emitting region (or by intervening matter) happens. Sources in which all produced photons get out are called *optically thin*. If the radiation process takes place in an *optically thick* source, significant self-absorption can happen, modifying the shape of the synchrotron spectrum. In the dense medium where synchrotron photons are emitted, a distribution of charges is also present. These charges function as absorption targets from the traveling photons.

The derivation of synchrotron self-absorption is complicated. By the principle of detailed balance, absorption is related to emission at each electron energy. The detailed analysis [443] gives the absorption coefficient as

$$a(\nu) = \text{const} \times B^{(p+2)/2} \times \nu^{-(p+4)/2} \tag{14.19}$$

for a power-law distribution of electrons in a source with a magnetic field strength B. The absorption coefficient has the dimension of length^{-1} and relates the isotropic production spectrum of Eq. 14.17 to the attenuation inside the source. The relation is given by Longair [445] as

$$\frac{\mathrm{d}I_\nu}{\mathrm{d}x} = -a_\nu I_\nu + \frac{f(\nu)}{4\pi}, \tag{14.20}$$

which has the solution

$$I_\nu(x) = \frac{f_\nu}{4\pi a_\nu}\left(1 - e^{-a_\nu x}\right). \tag{14.21}$$

A source of thickness ℓ is optically thin if $a_\nu \ell \ll 1$, in which case the differential power emitted toward the observer is $f_\nu \ell / 4\pi \propto \nu^{-s}$ with $s = (p-1)/2$. For an optically thick source, with $a_\nu \ell \gg 1$ it is instead

$$I_\nu = \frac{f_\nu}{4\pi a_\nu} \propto \nu^{5/2}, \tag{14.22}$$

independent of the slope of the electron spectrum. Another way to interpret the result is that, for an optically thick source, only the photons within one absorption length ($\Delta x \sim 1/a_\nu$) from the edge emerge. This distance increases with frequency so that at high frequency synchrotron radiation from the entire source emerges. Figure 14.3 shows the two asymptotic regimes. The observed spectrum will increase from low frequency, reach a maximum, and then fall with a slope s related to the spectral index of the electron spectrum that is driving the process.

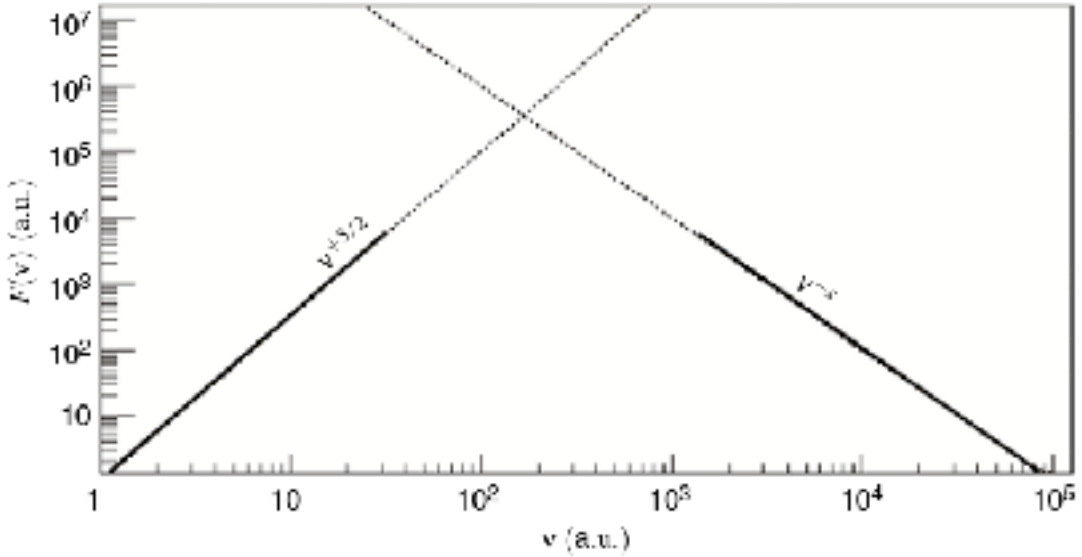

Figure 14.3 Impact of the synchrotron self-absorption on the synchrotron spectrum. Only asymptotic behaviors are given here.

14.1.2 Inverse-Compton scattering

The ultra-relativistic electrons (positrons) that produce the synchrotron component have a certain probability to scatter off ambient photons (synchrotron photons or others). The electron donates in the scattering some of its energy to the photon. This process enhances the energy of the photons via multiple up-scattering and it is called *inverse-Compton emission*, to be distinguished from the *direct* Compton scattering in which the electron is at rest and the photon scatters on the electron. For low photon energies $E_\gamma \ll m_e c^2$ the scattering from electrons at rest happens in the classical *Thomson* regime, which is regulated by the Thomson cross section for unpolarized incident radiation

$$\frac{\mathrm{d}\sigma_\mathrm{T}}{\mathrm{d}\Omega} = \frac{r_e^2}{2}(1 + \cos^2\theta) \tag{14.23}$$

and

$$\sigma_\mathrm{T} = \frac{8\pi}{3} r_e^2. \tag{14.24}$$

In these formulas, r_e is the classical electron radius; see Appendix A.1. The incident photon energy remains nearly unchanged ($E_{\gamma i} \sim E_{\gamma s}$) and the scattering is called *coherent* or *elastic*. When $E_\gamma \gg m_e c^2$ quantum effects become important, which alter the cross sections. The energy of the scattered photons changes $E_{\gamma i} \neq E_{\gamma s}$ because of the recoil of the charge and the scattering becomes *inelastic*. The regime in which inelastic scattering dominates is called *Klein–Nishina*, and it is regulated by the cross section [446]

$$\frac{\mathrm{d}\sigma_{KN}}{\mathrm{d}\Omega} = \frac{r_e^2}{2}\frac{E_{\gamma s}^2}{E_{\gamma i}^2}\left(\frac{E_{\gamma i}}{E_{\gamma s}} + \frac{E_{\gamma s}}{E_{\gamma i}} - \sin^2\theta\right). \tag{14.25}$$

The Klein–Nishina cross section is smaller than the Thomson cross section, hence the Compton scattering becomes less efficient at higher energies.

So far we have summarized Compton scattering in a frame in which the electron is initially at rest. When the electron is in motion it has some kinetic energy to be transferred to the photon via inverse-Compton scattering. In this way, a low-energy photon is converted to higher energy. In the rest frame of the energetic electron, the photon energy appears higher by a factor of the electron Lorentz factor γ. After the scattering, a transformation back to the lab system gives another factor of γ, so the photon energy is boosted by a net factor of γ^2. As long as the photon as seen in the rest frame of the electron is in the Thomson regime ($\gamma h\nu_0 <\sim 100\,\mathrm{keV}$), the photon can gain enormous energies via multiple up-scattering. When the intermediate photon reaches a larger energy, the quantum effects mentioned for the Klein–Nishina regime reduce the probability of scattering.

An important relation between the power in synchrotron radiation and that in inverse-Compton scattering for modeling of individual sources is [443]

$$\frac{P_{\mathrm{synch}}}{P_{\mathrm{comp}}} = \frac{U_B}{U_{\mathrm{ph}}}, \tag{14.26}$$

where $U_B = B^2/8\pi$ is the energy density in the magnetic field and U_{ph} is the energy density of photons. The relation holds if the photons are in the Thomson regime. It is sometimes useful in distinguishing between hadronic and leptonic models of sources.

14.2 Active galactic nuclei

A few per cent of all the galaxies present at a given time are characterized by a compact and extremely luminous central region, so bright that it outshines the rest of the galaxy. These objects are galaxies which host a so-called Active Galactic Nucleus (AGN). AGNs are characterized by a broad band emission from radio to >TeV γ-rays and strong time variability. They have been detected up to large distances ($z = 7.1$) and show a strong evolution, meaning that their power was higher in the past with a peak at $z \simeq 2$. The enormous amount of energy of AGNs (up to a bolometric luminosity $L_{\rm bol} \simeq 10^{47}$ erg/s $\simeq 3 \cdot 10^{13}\, L_\odot$) make them special laboratories for extreme physics – and also potential sources of ultra-high-energy cosmic rays.

AGNs are powered by the gravitational energy released in the accretion process around a supermassive black hole (see Section 13.3.2) hosted at the center of the galaxy. It is commonly believed that the central engine, a spinning black hole, is surrounded by the accretion disk and possibly by a further dusty torus. AGNs often show radiant powers L higher than their corresponding Eddington luminosities. From Eq. 13.21, for example, $L_{\rm Edd} \sim 10^{46}$ erg/s for a central black hole of $10^8\, M_\odot$.

If the environment around the BH supplies mass at a rate equal to $\dot{M}$ and the accretion process is stationary, an accretion disk is formed. Jets are formed parallel to the spin axis, powered by the gravitational energy released in the accretion disk (see Figure 14.4). Because of the jets, classification of AGNs is strongly affected by the viewing angle [447, 448].[1] The spectrum of AGNs is characterized by a non-thermal continuum, strong emission lines in the optical band, and radio emission from the jets. Depending on the intensity of these components, AGNs are classified in subclasses which are not always connected to the physical parameters of AGNs. If a prominent radio jet is observed, the AGN is defined as *radio-loud*, otherwise it is a *radio-quiet* AGN. This separation is done quantitatively using the *radio-loudness* defined as

$$R_L = \log\left(\frac{f_{5\mathrm{GHz}}}{f_{\mathrm{B}}}\right) \tag{14.27}$$

where $f_{5\mathrm{GHz}}$ and f_{B} correspond to the flux in radio at 5 GHz and in the optical B band. $R_L \geqslant 1$ is loud [447].

A second criterion used in the classification of AGNs is based on the optical part of the spectrum. *Type 1* AGNs present a bright continuum and emission lines, in contrast to *type 2* AGNs, which show a weak continuum and only narrow emission lines. A more detailed and complete description of the classification of AGNs is given in Ref. [450].

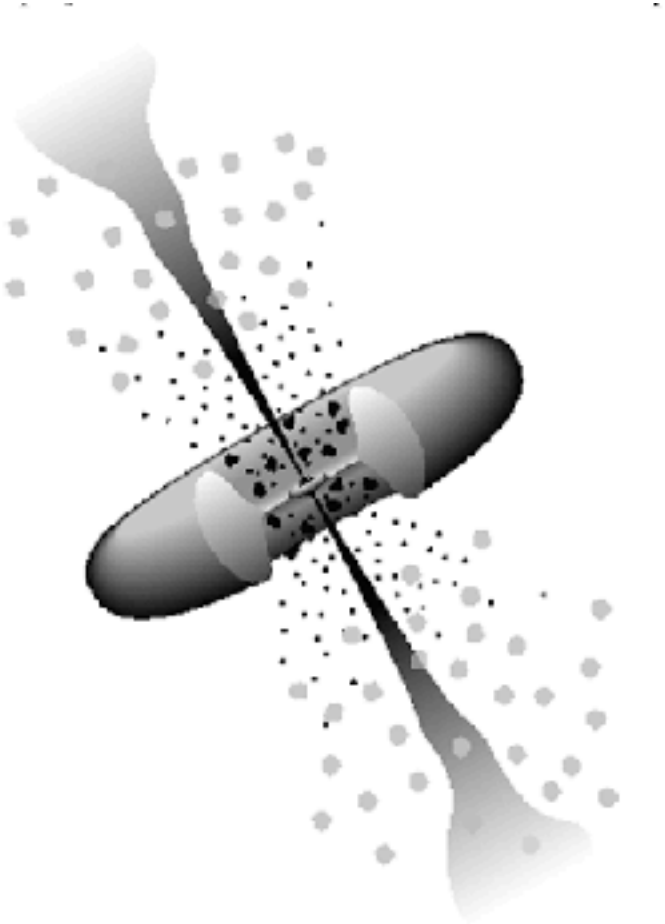

Centaurus A

Figure 14.4 Schematic and idealized view of a radio-loud AGN. The central black hole is surrounded by the accretion disk and the dusty torus. Jet-like emission of particles is also visible. From Urry and Padovani [447], a University of Chicago publication, © 1995 by the Astronomical Society of the Pacific, reproduced with permission.

SHADOW SIZE The Event Horizon Telescope captured the first image of M87's black hole. That image showed that the black hole's mass is about 6.5 billion times the mass of the sun, close to what astronomers expected based on the galaxy's stars.

EVENT HORIZON TELESCOPE COLLABORATION

The elliptical galaxy M87 is the home of several trillion stars, a supermassive black hole and a family of roughly 15,000 globular star clusters. For comparison, our Milky Way galaxy contains only a few hundred billion stars and about 150 globular clusters. The monstrous M87 is the dominant member of the neighboring Virgo cluster of galaxies, which contains some 2,000 galaxies. Discovered in 1781 by Charles Messier, this galaxy is located 54 million light-years away from Earth in the constellation Virgo. It has an apparent magnitude of 9.6 and can be observed using a small telescope most easily in May.

This Hubble image of M87 is a composite of individual observations in visible and infrared light. Its most striking features are the blue jet near the center and the myriad of star-like globular clusters scattered throughout the image.

14.2.1 Radio-loud AGNs: blazars

About 10–15% of all the AGNs are radio-loud ($R_L \geqslant 1$). The radio-loudness of AGNs is most probably related to the type of the host galaxy and to the spin of the black hole, which might trigger the production of the relativistic jets. When AGN's jets are oriented toward Earth with a small angle $\theta_{\rm obs}$, the object is called a *blazar*. At small $\theta_{\rm obs}$ relativistic effects are very important.[2] The name blazar comes from a combination of *BL Lacertae* (BL Lac) objects and quasars, reflecting the history of their discovery [452]. Blazars are known to accelerate particles to the highest observed energies. They are therefore of great interest for cosmic rays, gamma rays and neutrino astronomy. Blazars are relatively rare compared to all other types of AGN. Nevertheless they are detected at all frequencies and are the dominant population observed in the high-energy gamma ray band. At present, multi-frequency data of about 3,500 blazars have been collected from either confirmed blazars or objects exhibiting characteristics close to this type [453].

Two blazar classification schemes are present in the literature: the so-called *simplified view of blazars (BSV)* [454] based on the assumption that the maximum energy reached by the electrons does not depend on the luminosity of the blazar, and the *blazar sequence scenario* [455] where instead, the maximum energy of the electrons is supposed to be a strong function of the source luminosity. Depending on the presence or the lack of broad emission features (emission lines) in their optical spectrum, blazars are classified in *Flat-Spectrum Radio Quasars* (FSRQ) or in *BL Lacs* respectively [456]. However, on some occasions, well-established BL Lac objects have been found to exhibit emission lines, including BL Lacertae itself.

Understanding the observed spectra and variability of blazars is at present an active area of research. The low-energy hump is generally attributed primarily to synchrotron photons from relativistic electrons present in the jet. The higher-energy hump is produced most probably by a mixture of leptonic and hadronic processes. In a purely leptonic model, the high-energy photons populating the second hump are produced by up-scattering via the inverse-Compton effect. The low-energy target photons can be the synchrotron photons within the emission region (SSC = synchrotron self-Compton) [459, 460], or external photons (EC = external Compton), as for example from the accretion disk [461]. High-energy photons might also have a hadronic origin via the synchrotron emission from ultra-relativistic protons or via the interaction of the relativistic protons with the radiation fields within the emission region [462, 463]. These interactions produce high-energy neutral and charged pions. The neutral pions contribute to the high-energy photons via $\pi^0 \rightarrow \gamma + \gamma$ decay. The charged pions produce muons, electrons, positrons and neutrinos. The high-energy photons from decay of neutral pions are likely to cascade to lower energy by $\gamma + photon \rightarrow e^+ + e^-$, so they do not necessarily provide the majority of the high-energy γ-rays. The observation of TeV – PeV neutrinos, which are produced only by interactions of hadrons, is the most direct way to distinguish between the leptonic or hadronic nature of the most energetic blazars.

14.2.2 Example of a FSRQ blazar: 3C 279

The object 3C 279 hosts a compact, variable, flat-spectrum radio core. It has been the target of many multi-wavelength campaigns in order to investigate the physical conditions at the source and to shed light on the mechanisms operating in blazars. The source can vary by almost an order of magnitude in intensity between high and low states [465]. In Ref. [465], both states are fitted with an SSC model, with the configuration of the jet fixed while varying only the power and maximum energy of the accelerated electrons. The synchrotron peak and the high-energy IC peak are correlated. 3C 279 has been detected in the VHE γ-rays by the Major Atmospheric Gamma Ray Imaging Cherenkov (MAGIC) Telescope during an exceptional γ-ray flaring state [466], making it one of the most distant objects ever observed in the TeV band. In [467] the purely leptonic interpretation of the 3C 279 SED has been challenged, favoring a leptohadronic scenario [458]; see Figure 14.5.

The figure shows the lepto-hadronic fit of Ref. [458] to the data in the high state. The high-state data are shown with dark points, while the low-state data are shown in grey. The low-energy peak is accounted for as synchrotron radiation, but the high-energy component is accounted for up to 10^{25} Hz (40 GeV) almost entirely by proton synchrotron radiation, with the data at higher energy accounted for by synchrotron radiation from muons and charged pions. The paper notes that the self-absorbed synchrotron model does not account for the observed radio contribution at low energy, which they attribute to emission from more extended regions outside the radiative jets. The contribution from the π^0-initiated cascade is included in the line for e^+/e^- at high energy.

The fluxes of neutrinos from decay of charged pions and muons in 3C279 are also estimated in Ref. [458]. They use a calculation analogous to that described in Section 11.4 for neutrinos from the Milky Way and estimate a rate of $\sim$ 0.3 detected events per year from 3C279 in IceCube.

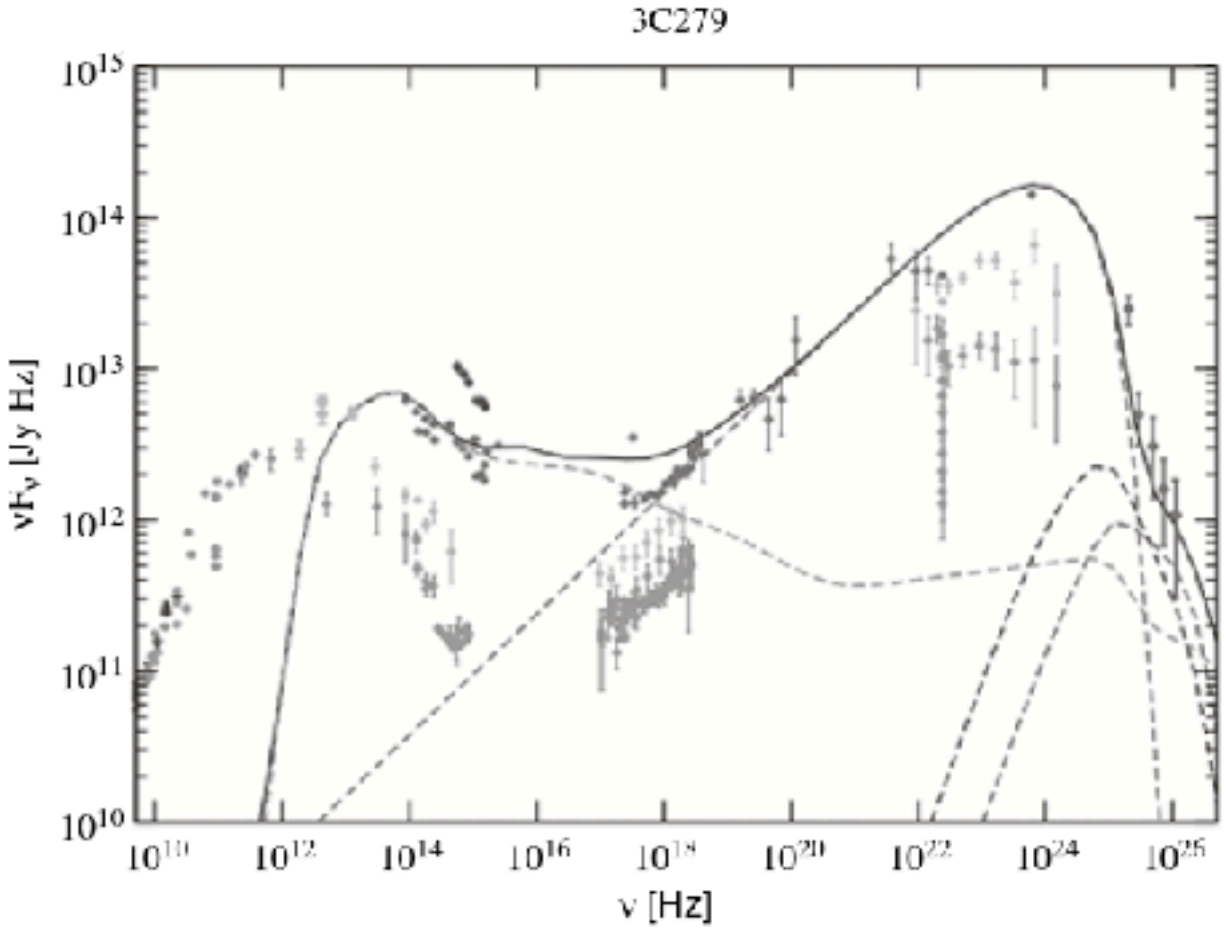

Figure 14.5 Equilibrium fit to the SED of 3C279. This figure from [458] also includes multi-wavelength data points from Ref. [464]. The model curves are: synchrotron emission from electrons/positrons (peak at 10^{13} Hz); proton synchrotron (peak at 10^{24} Hz); muon synchrotron (peak just below 10^{25} Hz); and pion synchrotron (peak just above 10^{25} Hz). The solid line shows total spectrum as the sum of these contributions. From [458], © 2015 by American Astronomical Society, reproduced with permission.

14.2.3 Example of a BL Lac blazar: Mrk 421

Because of its proximity and luminosity, Mrk 421 was the first BL Lac object detected in the high-energy γ-rays, by the Energetic Gamma Ray Experiment Telescope (EGRET) [471] at energies above 100 MeV. It was also the first extragalactic source detected with an imaging atmospheric Cherenkov telescope (Whipple [472]). Mrk 421 has a $\nu_S^{peak} > 10^{15}$ Hz and is therefore categorized as an HBL. The peak frequency of the high-energy hump is in the VHE regime.

Both leptonic and hadronic models can explain the observations, as illustrated in Figure 14.6. In the SSC model, a complex electron spectrum consisting of three components is used to fit the data: $p = 2.2$, 40 MeV–25 GeV; $p = 2.7$, 25 GeV–200 GeV; $p = 4.7$, 200 GeV–50 TeV. In the lepto-hadronic model both the electrons and the protons are assumed to have a hard spectral index of $p = 1.9$. The electron spectrum extends from 36 MeV to 20 GeV, while the proton spectrum extends from the proton rest mass to 2×10^{18} eV. The lepto-hadronic model assumes a much larger magnetic field of 50 G, compared to less than 0.1 G for the SSC model. In both cases the acceleration occurs in a relativistic jet which gives a Doppler boost > 10. In the lepto-hadronic model, the high-energy cascade is initiated by interactions of protons in the synchrotron radiation peak.

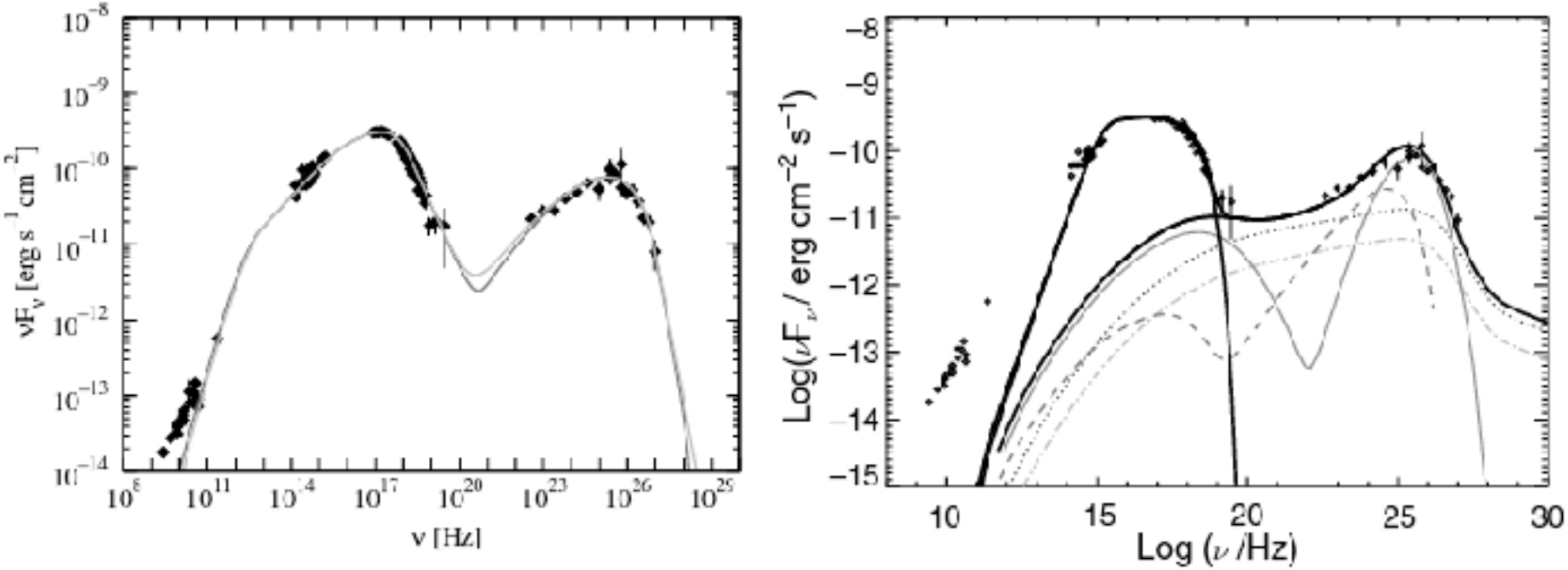

Figure 14.6 SED of Mrk 421. Data from Fermi and MAGIC averaged over the period 19 January 2009 - 1 June 2009 [468]. Left: SSC model using the one-zone SSC code of [469]; Right: lepto-hadronic model using the synchrotron-proton blazar model of [470] (see text for explanation of the lines). From [469] and [470], © 2010 & 2002 by American Astronomical Society, reproduced with permission.

It is interesting to see how the various products of the proton cascade contribute to the photon spectrum, as shown by the broken lines in the right panel of Figure 14.6. The dotted line, which is the dominant contribution between the peaks, is the π^0-initiated cascade. Parallel to it but lower is the cascade contribution from decay products of charged pions. Unlike the case for hadronic models of SNR (e.g. Tycho in Figure 13.10), here the π^0 cascade does not give the main contribution in the GeV range and above. Instead, the dominant contribution to the high-energy peak is proton synchrotron radiation up into the GeV region (double-humped dashed curve) and muon synchrotron radiation at the highest energy (the triple-dot-dashed line).

The ultimate proof for the existence of high-energy protons in blazar jets can come from a positive detection of high-energy neutrinos, which has not yet been accomplished. A comparison between a lepto-hadronic interpretation of the Mkn 421 and one of the high-energy neutrino events detected recently by IceCube [327] is shown in Figure 14.7. (IceCube Event 9 is a cascade event with an estimated energy of 63 ± 8 TeV.) At present there are insufficient data to confirm or reject this possibility. This figure shows the π^0 component at production (before cascading) as the highest dashed peak on the right. Predicted neutrino fluxes are also shown.

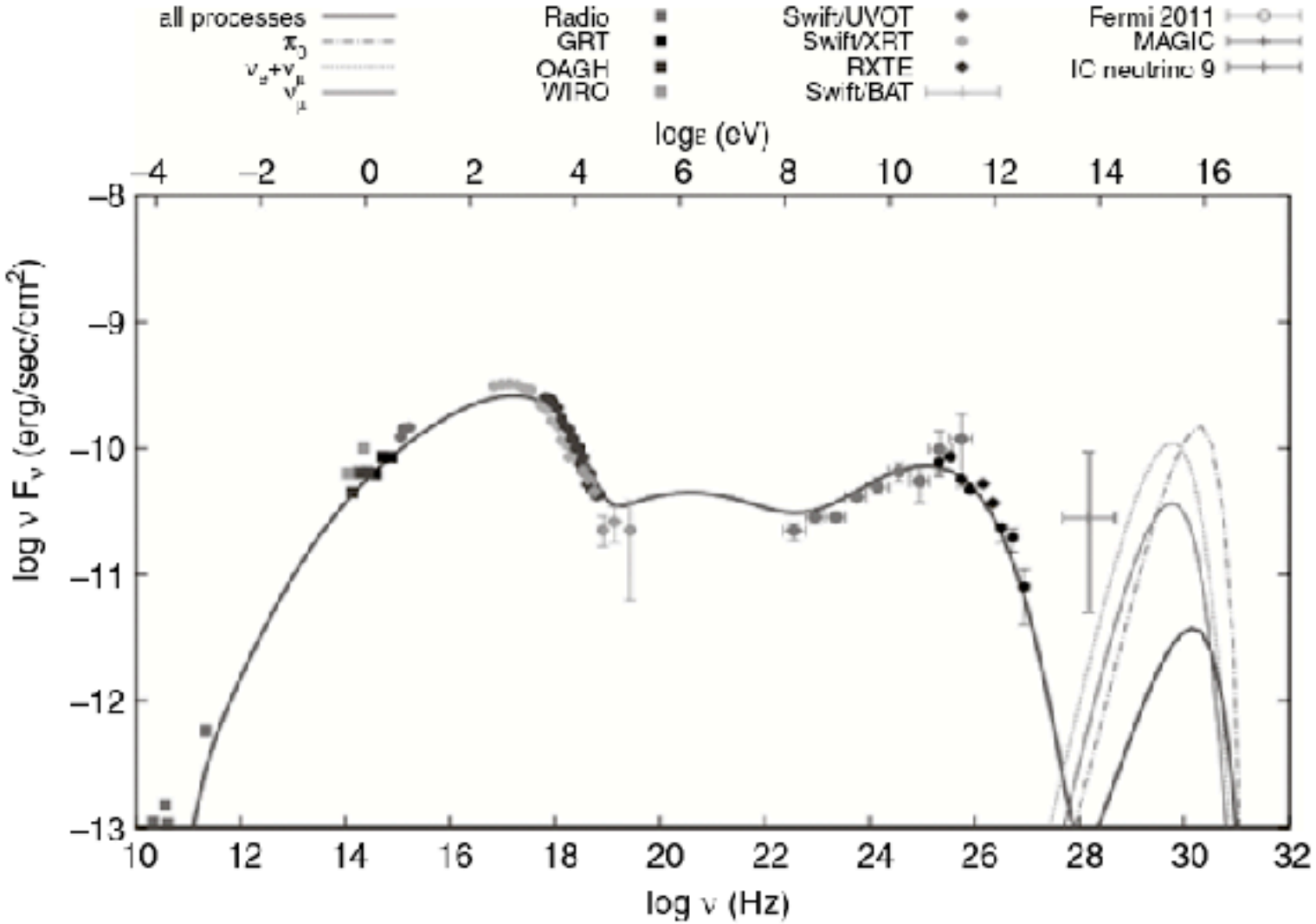

Figure 14.7 Figure taken from [473]: SED of Mrk 421, same data as in Figure 14.6. Shown are the model SED (black line) and the expected neutrino spectra. The IceCube neutrino event ID 9 is also shown [327].

14.3 Gamma ray bursts

Gamma ray bursts (GRBs) were discovered serendipitously in the late 1960s by the Vela satellites, originally designed to search for very fast and intense bursts of gamma rays produced by nuclear weapon tests in space [474]. GRBs are the most energetic transient events in the Universe, with an emitted energy up to 10^{53} erg. They are isotropically distributed, and hence extragalactic, as first observed by the Burst and Transient Experiment (BATSE) on the Compton Gamma ray Observatory (CGRO) [475]. GRBs show a highly variable temporal profile with $\delta T/T \sim 10^{-2}$, which still challenges present models. For a detailed review see e.g. [476].

Two wide categories of prompt emission are traditionally identified: long bursts ($t > 2\,\mathrm{s}$) and short ones ($t < 2\,\mathrm{s}$). A physical basis for the distinction is emerging connected to the progenitor type: collapsar or non-collapsar [477]. Long bursts are most probably connected to the catastrophic deaths of a massive star collapsing into a black hole [478], while the short ones may correspond to the merger of compact object binaries [479, 480]. Both types of emission are followed by a longer-lived *afterglow* radiation. The first detection of afterglows from long GRBs was obtained by the Beppo-SAX satellite in 1997, eight hours after the main burst of GRB 970228. The X-ray transient was followed up by a multi-wavelength campaign that revealed a fading transient at the position of the GRB [481]. An afterglow is consistent with the picture of the slowing down of a relativistic flow as it expands into the surrounding medium. Observations of afterglows can provide key information about the host galaxy, the distance and precise positioning of the GRBs.

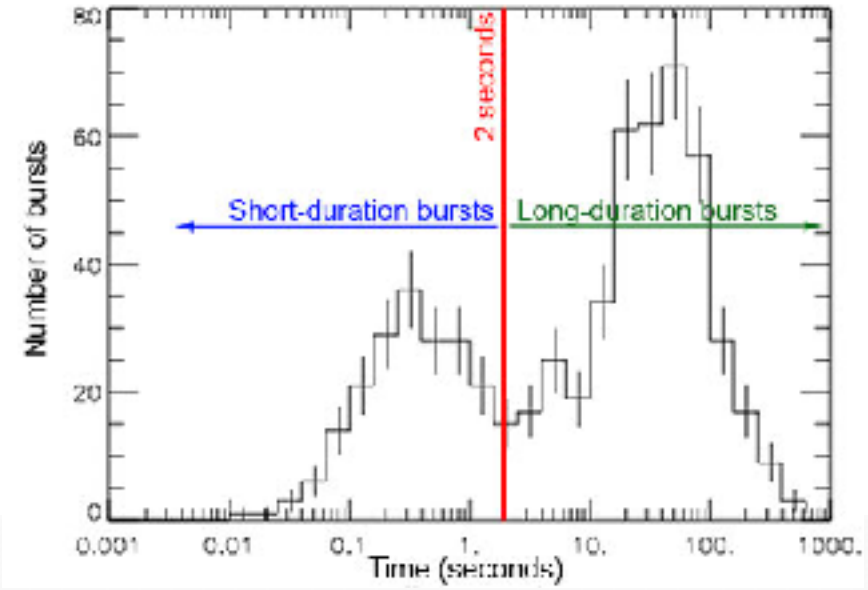
Number of bursts
Time (seconds)
2 seconds
Short-duration bursts
Long-duration bursts
0
20
40
60
80
0.001
0.01
0.1
1.
10.
100.
1000.

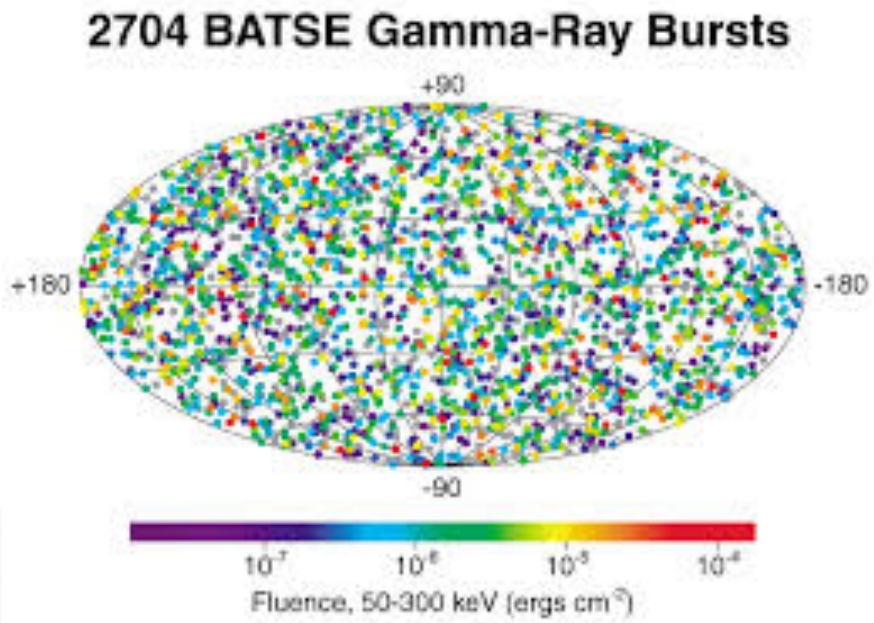
2704 BATSE Gamma-Ray Bursts
+90
+180
-180
-90
Fluence, 50-300 keV (ergs cm⁻²)

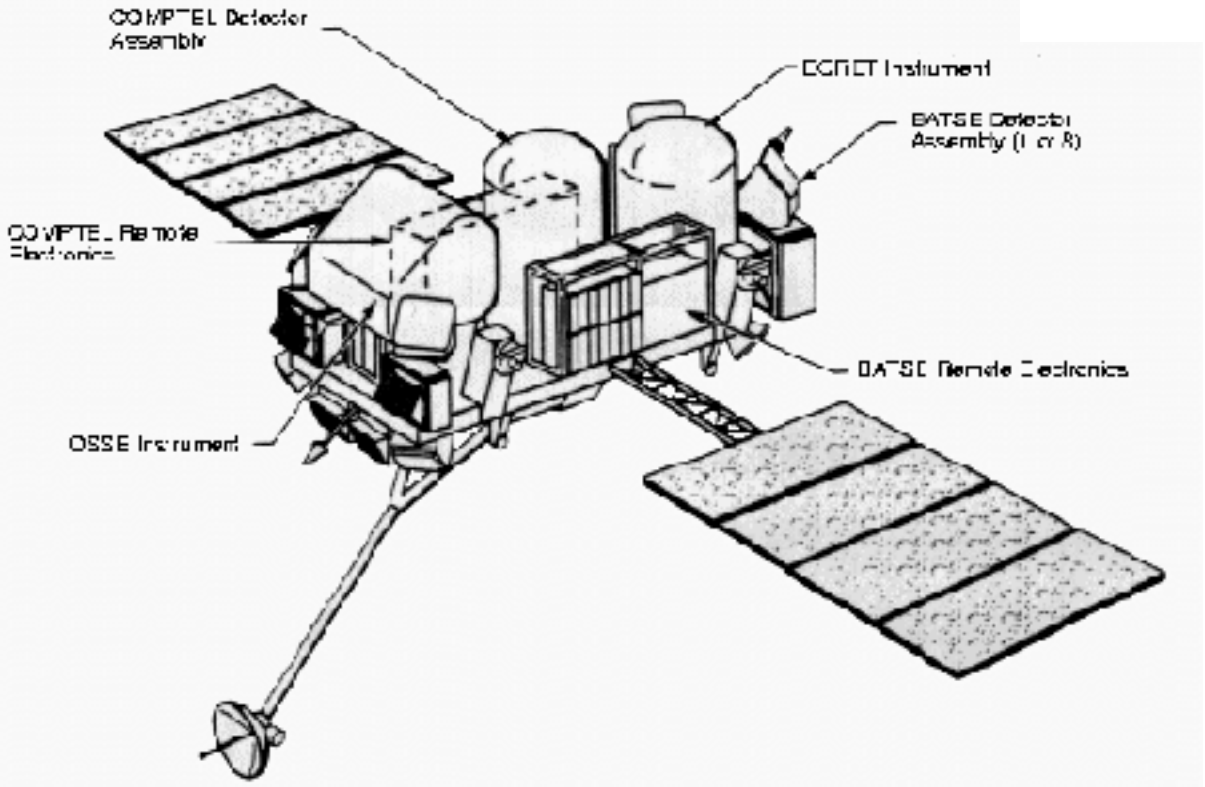
COMPTEL Detector Assembly
EGRET Instrument
BATSE Detector Assembly (1 of 8)
COMPTEL Remote Electronics
BATSE Remote Electronics
OSSE Instrument

14.3.1 *Collapsars: long gamma ray bursts*

Collapsars are powered by accretion of a massive disk formed around the black hole [482]. Relativistic jets are formed which punch through the outer layers of the progenitor and then into the surrounding medium as illustrated in Figure 14.8. This scenario has found observational support through the association of GRB afterglows with their progenitor core-collapses. The first direct evidence of the GRB/core-collapse connection was gained through the study of the relatively close by GRB 030329 ($z = 0.1685$) and its associated very energetic type Ic supernova (*hypernova*) SN2003dh [483]. The supernova light curve emerged from the GRB afterglow within ten days and was spatially coincident with the GRB. The broad lines in the supernova spectrum indicate an initial expansion velocity of more than $\approx 36,000$ km/s.

Three principle phases are identified in the *collapsar model*:

- Massive star core-collapse: a massive star ($M > 30 M_\odot$) with an iron core (1-2 $M_\odot$) undergoes a core-collapse. This results in formation of a black hole, either directly or via an accretion phase.
- Accretion disk formation: around the collapsed core a cylindrically symmetric accretion disk is formed with its symmetry axis parallel to the rotation axis. The disk accretes at a rate of about 0.5 $M_\odot$/s, amplifying entrained magnetic fields and injecting energy into the surrounding medium.
- Jet initiated fireball: matter is expelled preferentially along the rotational axes in form of a two-sided jet ($\theta_{\rm jet} < 10^\circ$), sometimes referred to as *fireballs*.

The existence of jets in GRBs is inferred from the study of the light curves of the afterglows and from polarization studies [484].

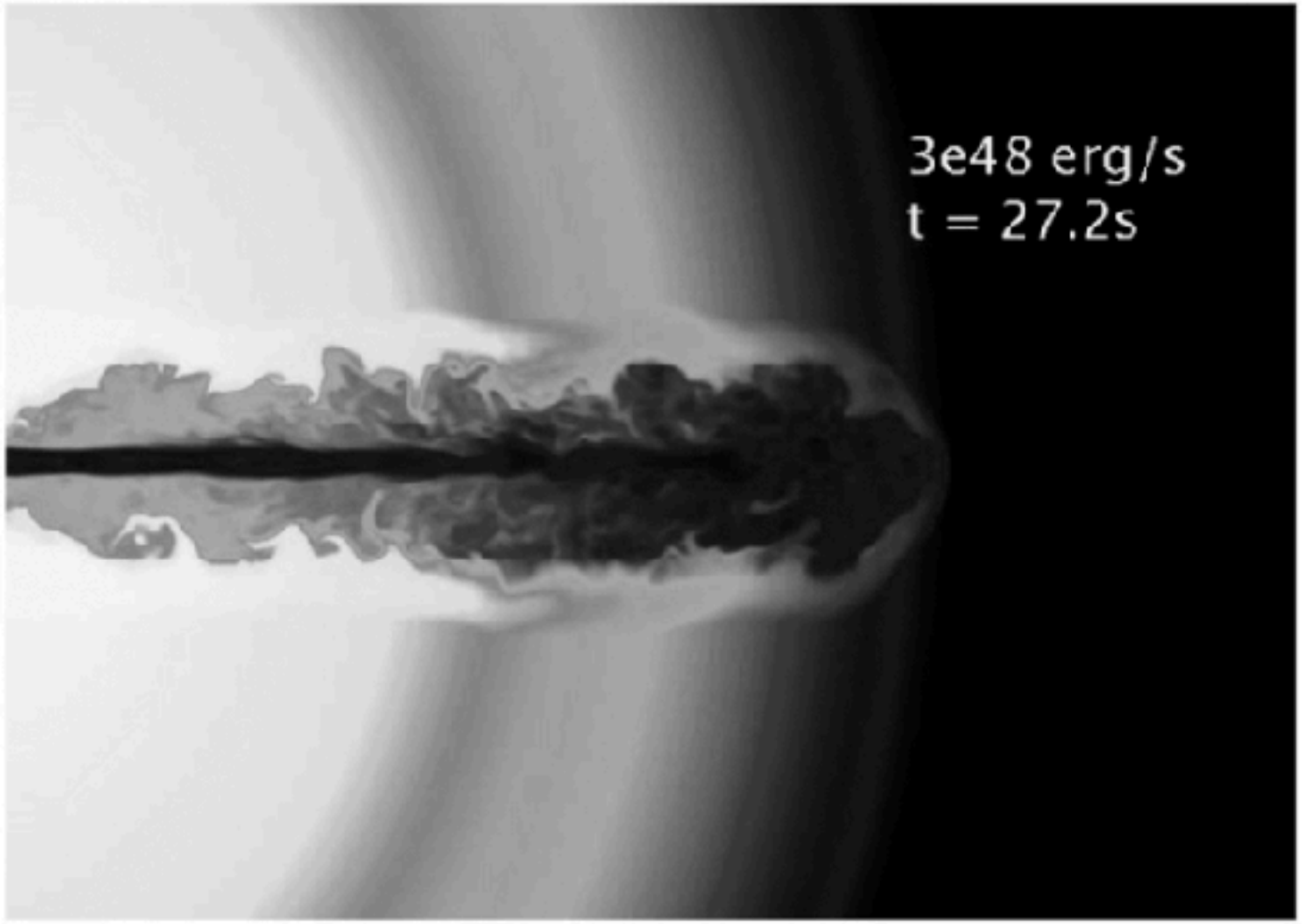

Figure 14.8 Three-dimensional modelling of a relativistic jet injected from the center of a 15 $M_\odot$ Wolf–Rayet star. Picture taken from [476].

From a supernova to a gamma-ray burst

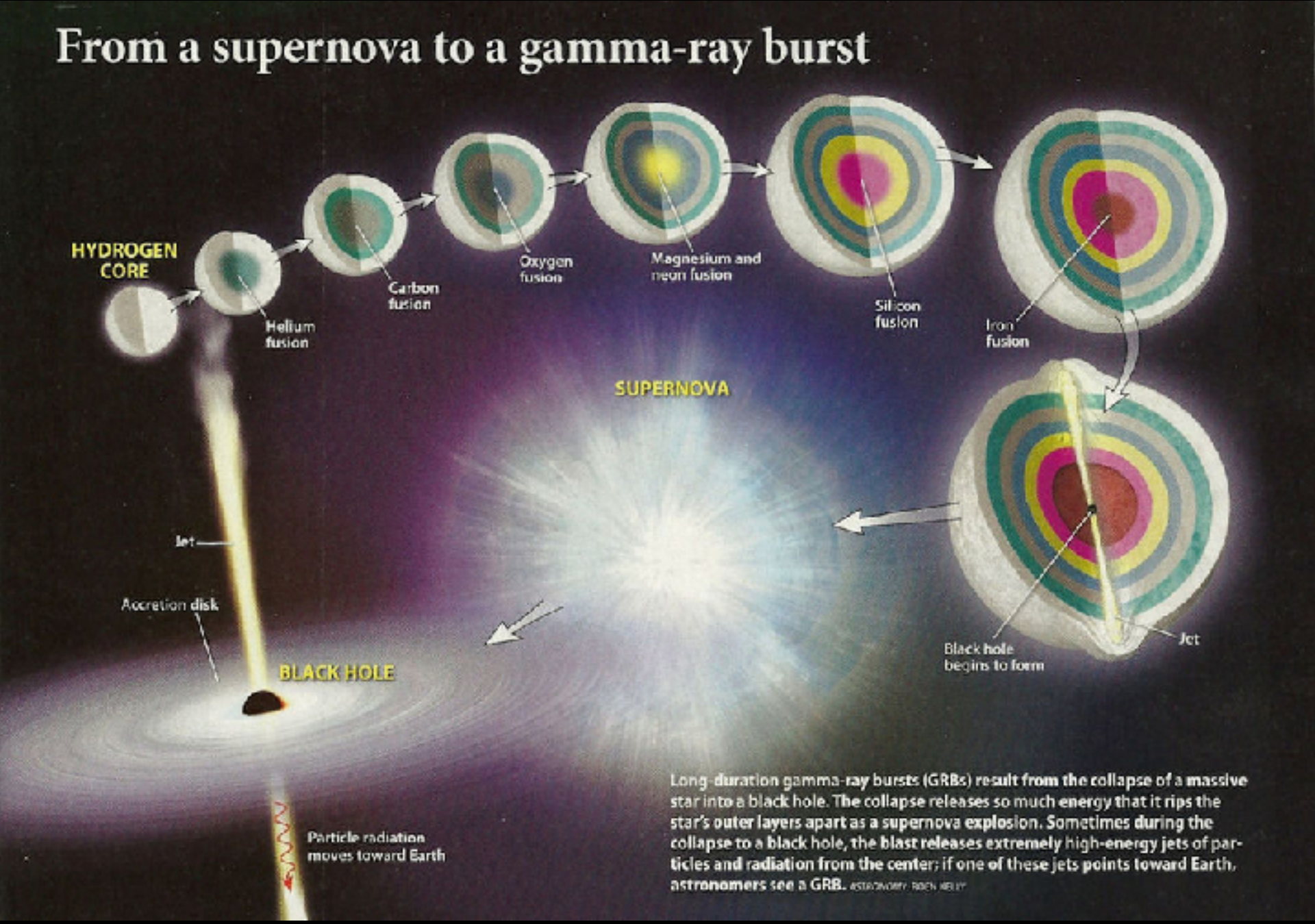

Long-duration gamma-ray bursts (GRBs) result from the collapse of a massive star into a black hole. The collapse releases so much energy that it rips the star's outer layers apart as a supernova explosion. Sometimes during the collapse to a black hole, the blast releases extremely high-energy jets of particles and radiation from the center; if one of these jets points toward Earth, astronomers see a GRB. ASTRONOMY: ROEN KELLY

14.3.2 Non-collapsars: short gamma ray bursts

Short GRBs are also cosmological in origin, and they show an afterglow emission similar to that of the long GRBs but less luminous. Lacking an association to a precursor supernova and given the short duration (down to tens of milliseconds), it is believed that the progenitors of the short GRBs are not massive stars but compact systems. Hence, short GRBs are considered to result from the merger of compact object binaries, two neutron stars (NS-NS) or a neutron star and a black hole (NS-BH) [479, 480]. Evidence of collimated emission is obtained from the study of spectral breaks in the light curves. Figure 14.9 illustrates stages in the merger of two neutron stars.

First Cosmic Event Observed in Gravitational Waves and Light

Colliding Neutron Stars Mark New Beginning of Discoveries

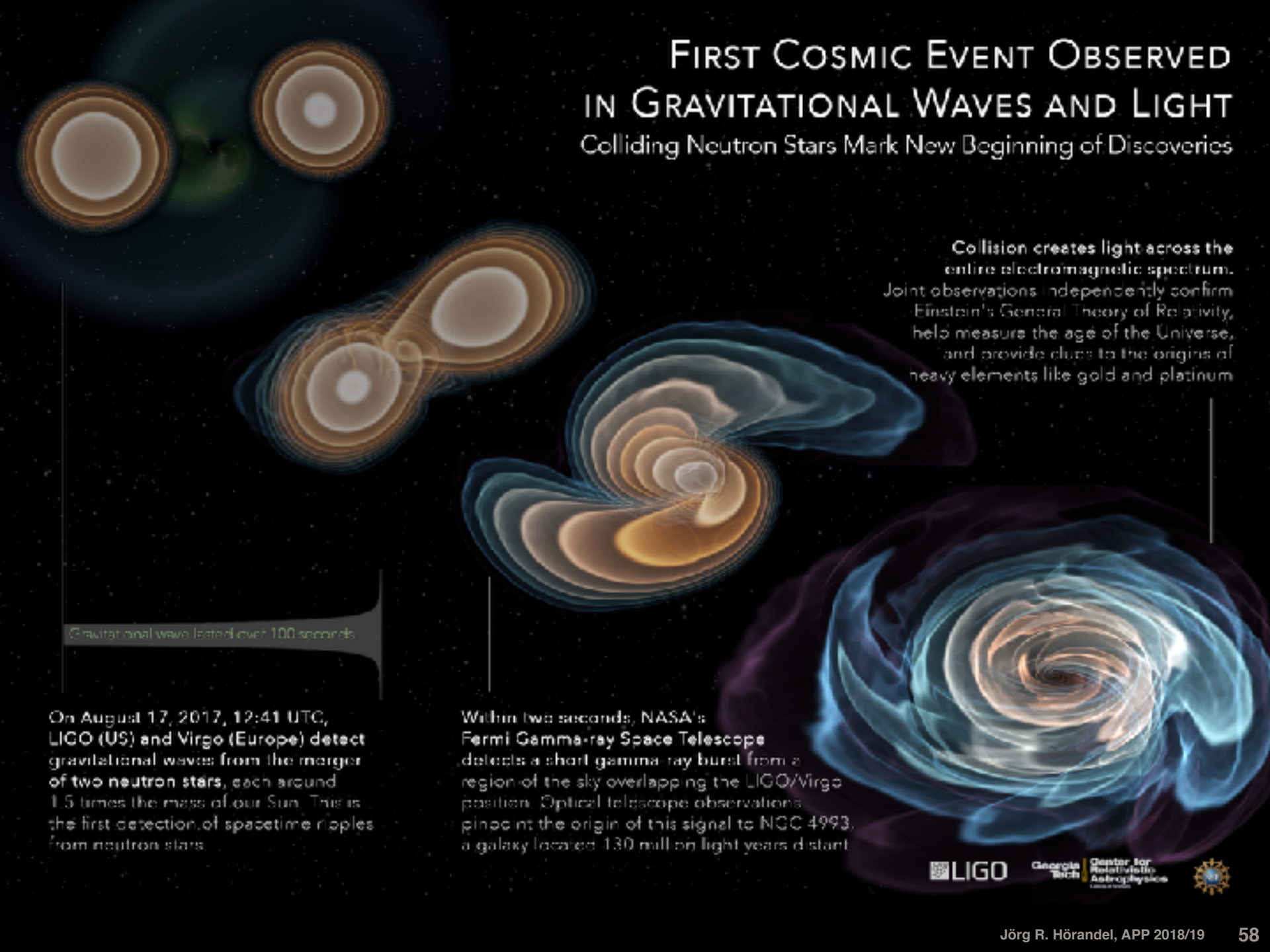

Fermi

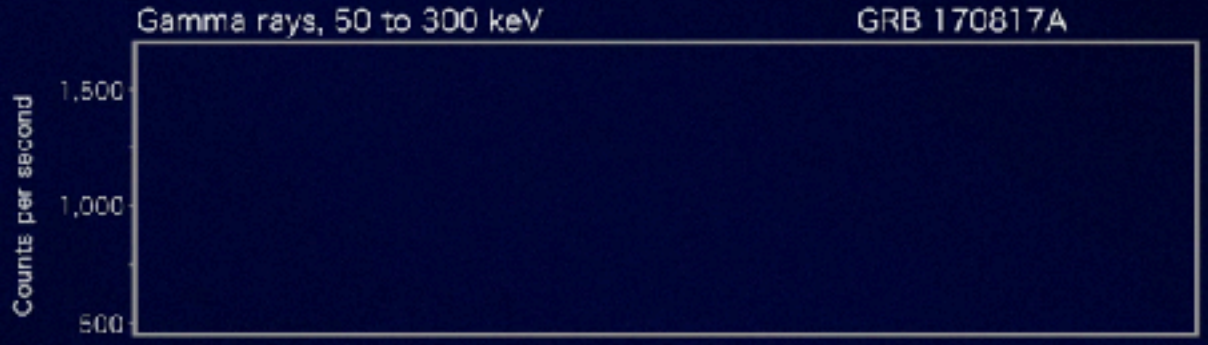
Gamma rays, 50 to 300 keV
GRB 170817A
Counts per second
1,500
1,000
500

LIGO

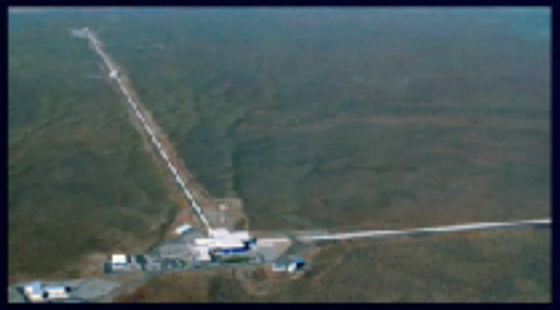

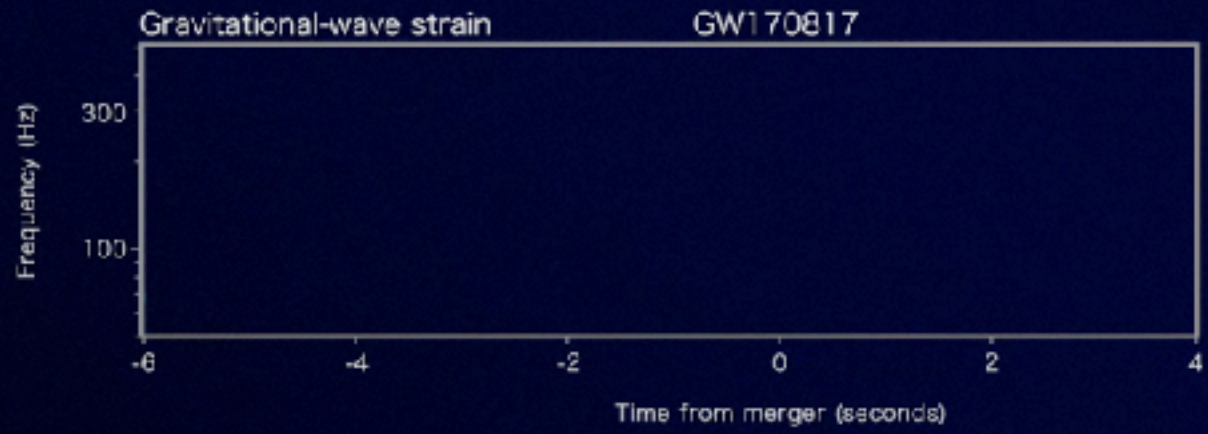
Gravitational-wave strain
GW170817
Frequency (Hz)
300
100
-6
-4
-2
0
2
4
Time from merger (seconds)

Kilonova

A kilonova is a transient astronomical event

merging of NS-NS or NS-BH

—> short GRBs + gravitational waves

—> strong electromagnetic radiation due to radioactive decay of r-process nuclei
(heavy nuclei)

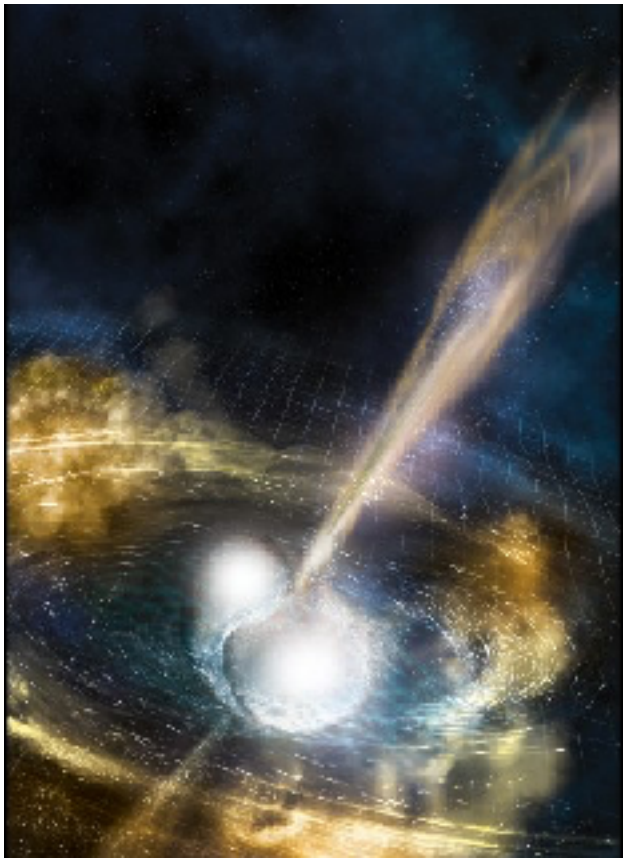

r-process

rapid neutron capture process

nucleosynthesis of atomic nuclei heavier than iron

very fast neutron capture, faster then beta decay

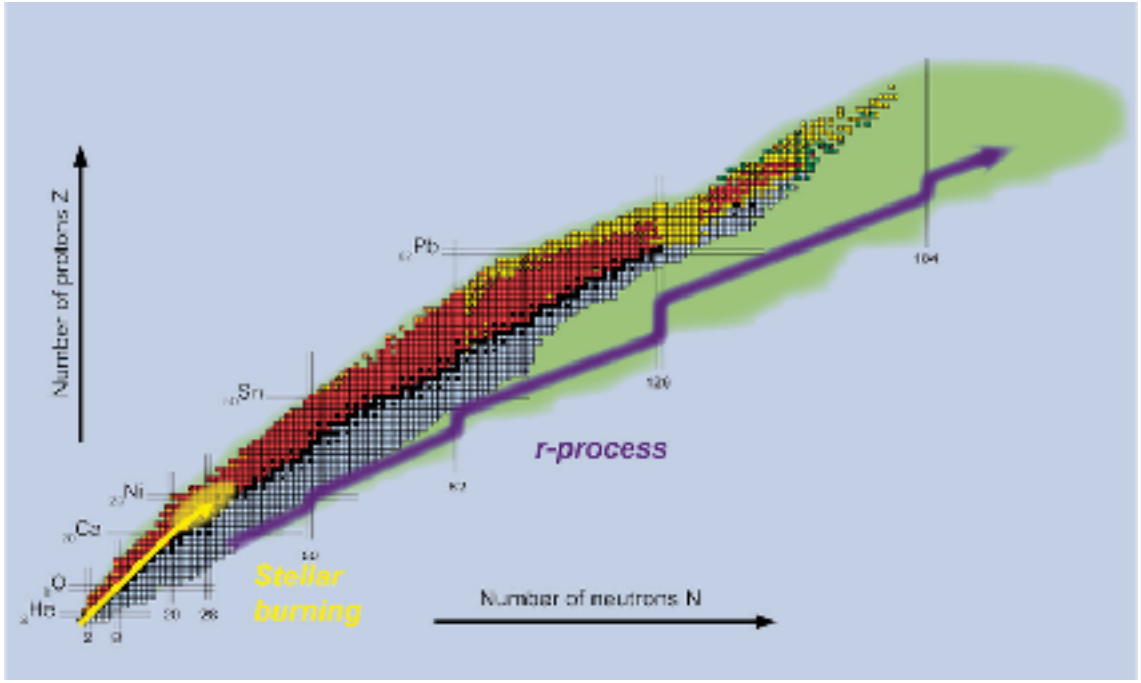

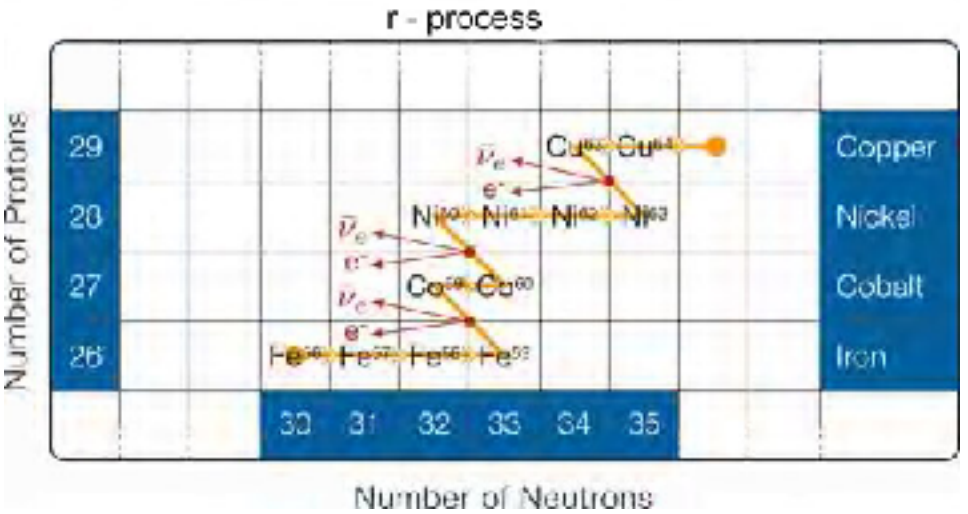

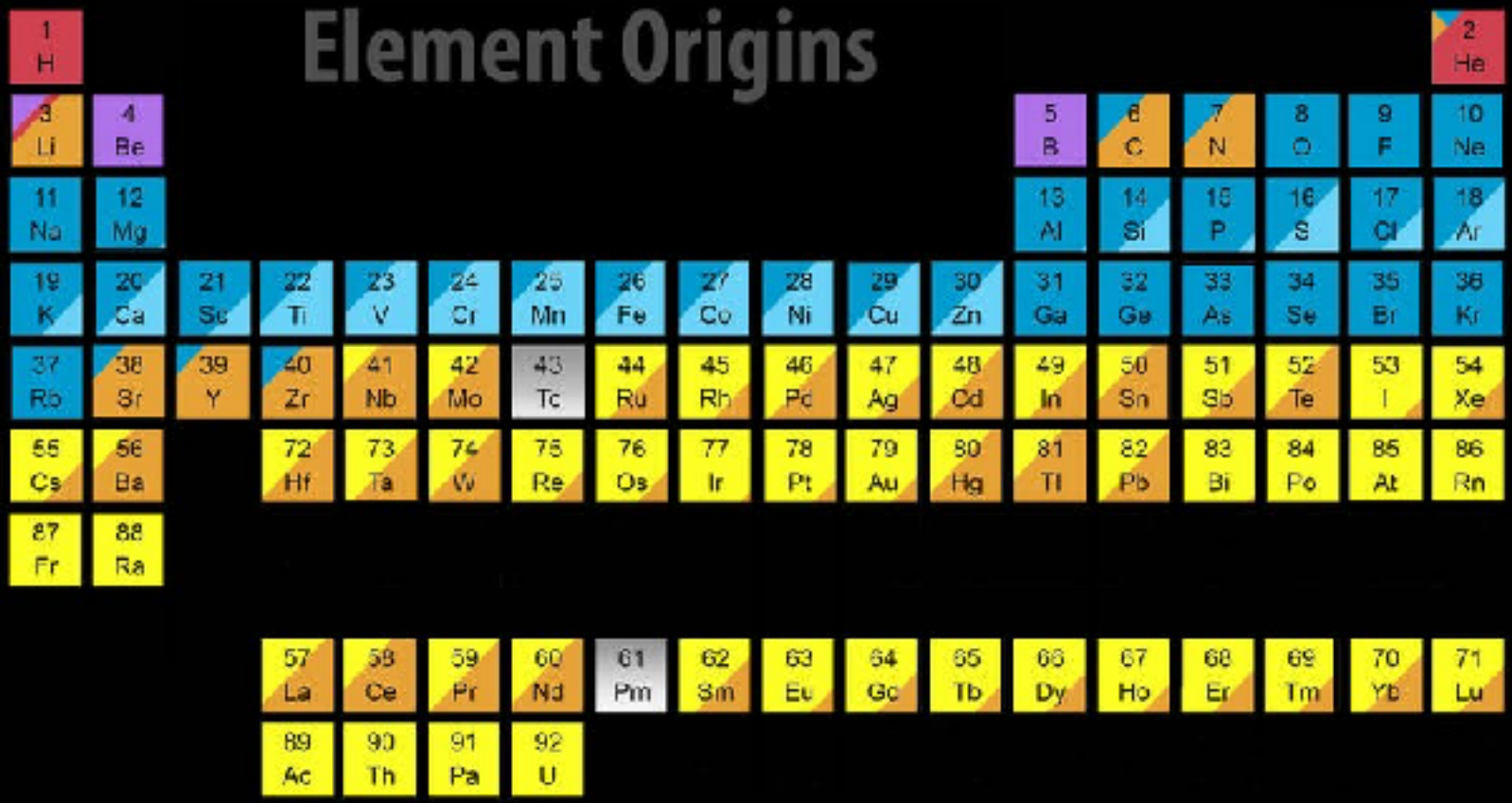
Element Origins
1 H
2 He
3 Li
4 Be
5 B
6 C
7 N
8 O
9 F
10 Ne
11 Na
12 Mg
13 Al
14 Si
15 P
16 S
17 Cl
18 Ar
19 K
20 Ca
21 Sc
22 Ti
23 V
24 Cr
25 Mn
26 Fe
27 Co
28 Ni
29 Cu
30 Zn
31 Ga
32 Ge
33 As
34 Se
35 Br
36 Kr
37 Rb
38 Sr
39 Y
40 Zr
41 Nb
42 Mo
43 Tc
44 Ru
45 Rh
46 Pd
47 Ag
48 Cd
49 In
50 Sn
51 Sb
52 Te
53 I
54 Xe
55 Cs
56 Ba
72 Hf
73 Ta
74 W
75 Re
76 Os
77 Ir
78 Pt
79 Au
80 Hg
81 Tl
82 Pb
83 Bi
84 Po
85 At
86 Rn
87 Fr
88 Ra
57 La
58 Ce
59 Pr
60 Nd
61 Pm
62 Sm
63 Eu
64 Gd
65 Tb
66 Dy
67 Ho
68 Er
69 Tm
70 Yb
71 Lu
89 Ac
90 Th
91 Pa
92 U
Merging Neutron Stars
Exploding Massive Stars
Big Bang
Dying Low Mass Stars
Exploding White Dwarfs
Cosmic Ray Fission

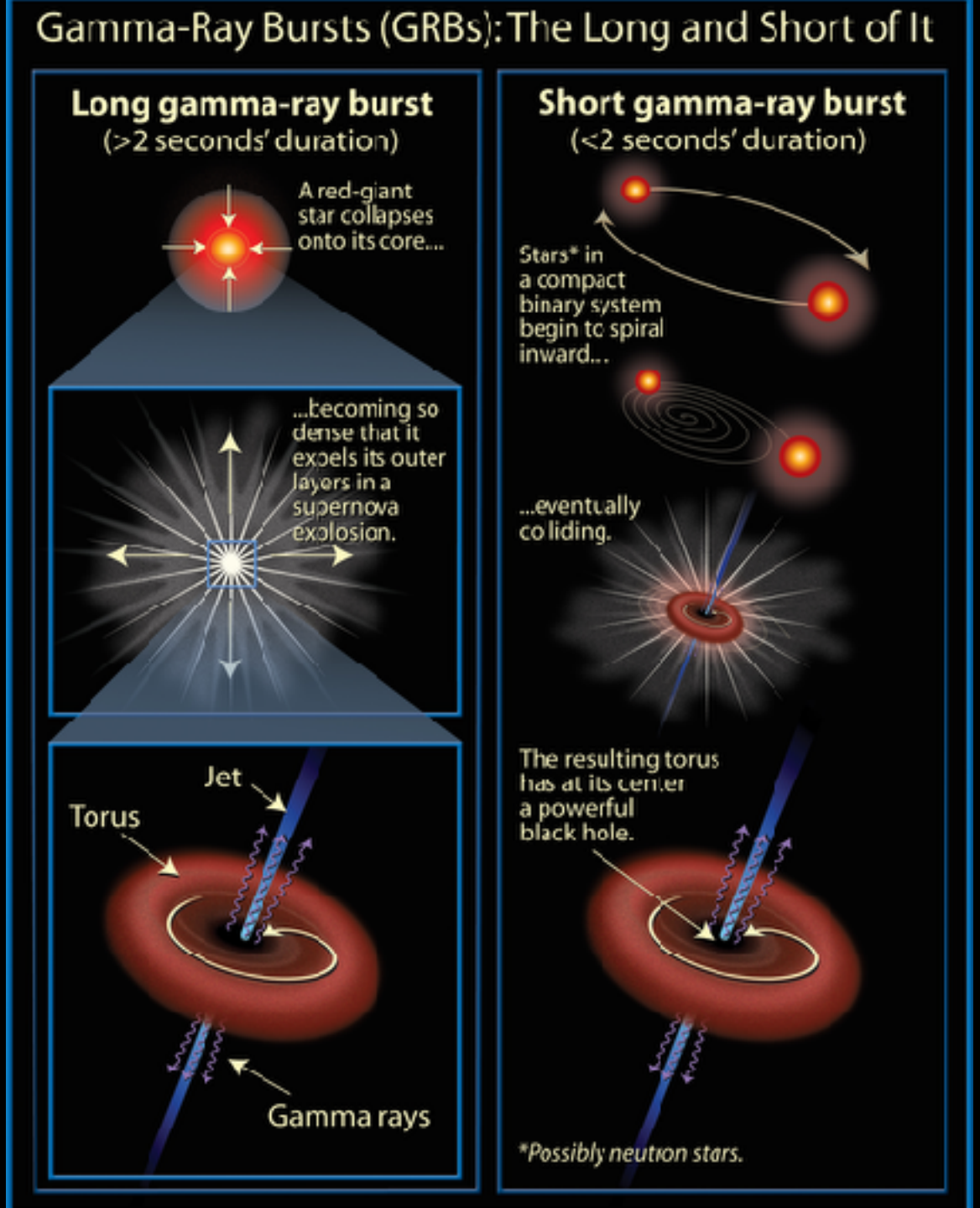
Gamma-Ray Bursts (GRBs): The Long and Short of It
Long gamma-ray burst
(>2 seconds' duration)
A red-giant star collapses onto its core....
...becoming so dense that it expels its outer layers in a supernova explosion.
Jet
Torus
Gamma rays
Short gamma-ray burst
(<2 seconds' duration)
Stars* in a compact binary system begin to spiral inward...
...eventually colliding.
The resulting torus has at its center a powerful black hole.
*Possibly neutron stars.

14.3.3 *Physical processes in gamma ray bursts*

The physics of the GRB prompt emission is still not understood in full detail. The primary uncertainties concern: whether the composition of the ejecta are matter (baryon) dominated or electromagnetically dominated (Poynting flux); whether the energy dissipation is via internal or external shocks; and whether the radiative mechanisms are synchrotron, synchrotron self-Compton or Comptonization of thermal photons. For reviews we refer to [485, 771].

The spectral analyses of many GRBs shows that the emission is non-thermal and follows the empirical "Band" function [486], a double broken power law

$$N_E(E) \propto \begin{cases} E^{\alpha} \exp(-E/E_0) & E < E_0 \\ E^{\beta} & E > E_0 \end{cases} \qquad (14.28)$$

with the parameters $\alpha > \beta$ and E_0 which vary from burst to burst. Typical values are $\alpha \approx -1$ and $\beta \approx -2$. Although the spectrum of GRBs varies strongly from burst to burst, the fact that the Band function can explain the majority of the spectra implies a possible common physical origin of the burst emission. The Band function can describe both thermal and non-thermal processes, but the physical origin is not yet understood. Relativistic shocks are formed which contribute to the acceleration of particles from the plasma. Shocks can be *external* if they occur in interaction with the interstellar material or *internal* if in shells formed in the GRB itself. Internal shock scenarios [487] are more powerful and therefore more interesting for the topic of high-energy emission.

Discussion: In her review [450], Julia Becker Tjus describes the three phases in which neutrinos could be produced in GRBs. In the precursor phase (dark area in Figure 14.10), calculations [493, 494] predict the main neutrino signal to extend up to several TeV. In the afterglow phase, ultra-high-energy cosmic rays may be present to interact and photo-produce neutrinos of very high energy, ~EeV [495]. During the main phase (medium grey region in Figure 14.10), the neutrino spectrum mirrors the Band spectrum of the target photons [492], and neutrinos in the 100 TeV range and somewhat above are predicted. This is a consequence of the importance of the Δ-resonance in photo-pion production (see Figure 4.22). Since the neutrino energy is proportional to the energy of the proton that produces it ($E_\nu \sim 0.05 \times E_p$), representing the cross section by a delta function at the Δ resonance leads to the condition $E_\gamma \cdot E_\nu = \text{const}$. Lower-energy neutrinos are produced from interactions with higher-energy photons (spectral index $\beta \approx -2$), while higher-energy neutrinos are produced from the lower-energy part of the photon distribution with spectral index $\alpha \approx -1$.

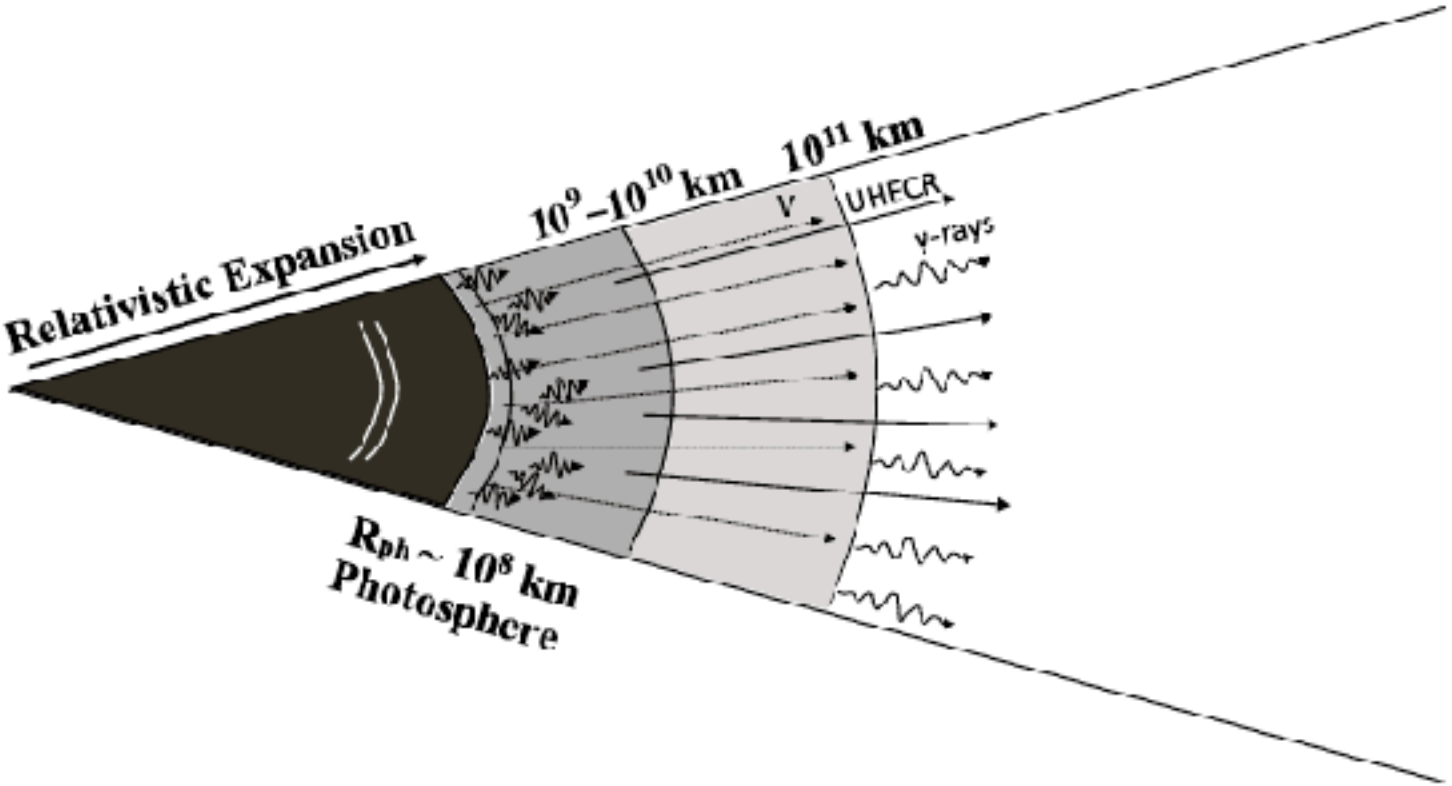

Figure 14.10 Schematic illustration of a GRB: the radiation dominated phase is represented in dark grey and it is followed by progressively more transparent phases. Following [491] high-energy neutrinos, ultra-high-energy cosmic rays (UHECR) and γ-rays are emitted at different radii.

The paper of Bustamante et al. [491] follows the neutrino production through the evolution of the burst to identify the distances from the explosions at which neutrinos, cosmic rays and γ-rays emerge. Their results are shown in Figure 14.11. The detailed calculation of Globus et al. [497] considers the acceleration of nuclei in GRBs in addition to protons. This model has interesting consequences for the origin of UHECR, which we discuss in Chapter 17.

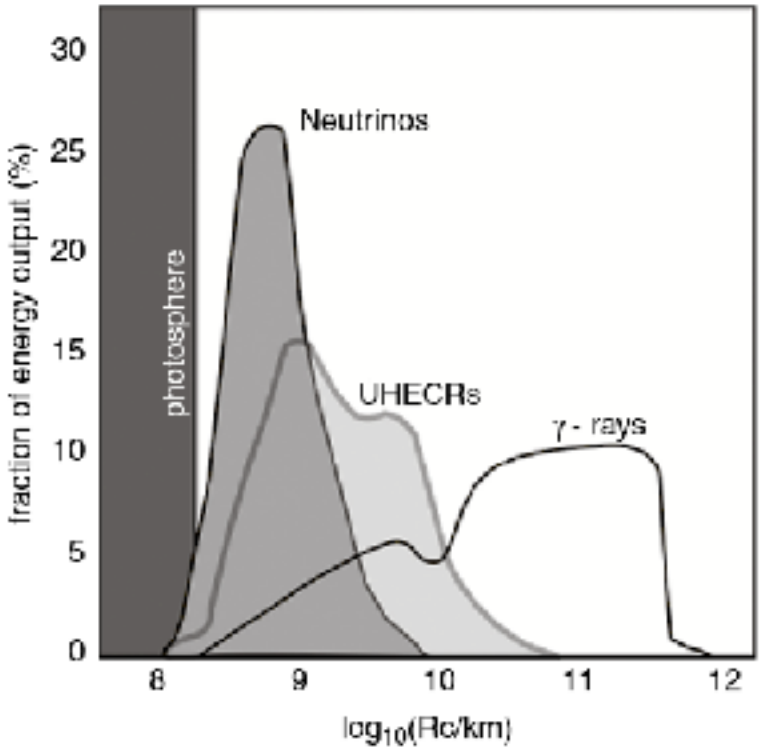

Figure 14.11 Figure modified from [491]: Fraction of the energy dissipated in prompt γ-rays, neutrinos and UHECR beyond the photosphere at different collision radius.